Gaia and Hubble Unveil the Kinematics of Stellar Populations in the Type II Globular Clusters ω Centauri and M22

G. Cordoni[1] , A. P. Milone[1,2] , A. F. Marino[1,2,3] , G. S. Da Costa[4] , E. Dondoglio[1], H. Jerjen[4] , E. P. Lagioia[1] ,
A. Mastrobuono-Battisti[5] , J. E. Norris[4] , M. Tailo[1], and D. Yong[4,6]

[1] Dipartimento di Fisica e Astronomia "Galileo Galilei"—Univ. di Padova, Vicolo dell'Osservatorio 3, Padova, IT-35122, Italy; giacomo.cordoni@phd.unipd.it
[2] Istituto Nazionale di Astrofisica—Osservatorio Astronomico di Padova, Vicolo dell'Osservatorio 5, Padova, IT-35122, Italy
[3] Centro di Ateneo di Studi e Attività Spaziali "Giuseppe Colombo"—CISAS, Via Venezia 15, Padova, IT-35131, Italy
[4] Research School of Astronomy and Astrophysics, Australian National University, Canberra, ACT 0200, Australia
[5] Department of Astronomy and Theoretical Physics, Lund Observatory, Box 43, SE–221 00, Lund, Sweden
[6] ARC Centre of Excellence for Astrophysics in Three Dimensions (ASTRO-3D), Canberra, ACT 0200, Australia

Abstract

The origin of multiple stellar populations in globular clusters (GCs) is one of the greatest mysteries of modern stellar astrophysics. *N*-body simulations suggest that the present-day dynamics of GC stars can constrain the events that occurred at high redshift and led to the formation of multiple populations. Here, we combine multiband photometry from the Hubble Space Telescope (HST) and ground-based facilities with HST and Gaia Data Release 2 proper motions to investigate the spatial distributions and the motions in the plane of the sky of multiple populations in the Type II GCs NGC 5139 (ω Centauri) and NGC 6656 (M22). We first analyzed stellar populations with different metallicities. Fe-poor and Fe-rich stars in M22 share similar spatial distributions and rotation patterns and exhibit similar isotropic motions. Similarly, the two main populations with different iron abundance in ω Centauri share similar ellipticities and rotation patterns. When different radial regions are analyzed, we find that the rotation amplitude decreases from the center toward the external regions. Fe-poor and Fe-rich stars of ω Centauri are radially anisotropic in the central region and show similar degrees of anisotropy. We also investigate the stellar populations with different light-element abundances and find that their N-rich stars exhibit higher ellipticity than N-poor stars. In ω Centauri both stellar groups are radially anisotropic. Interestingly, N-rich, Fe-rich stars exhibit different rotation patterns than N-poor stars with similar metallicities. The stellar populations with different nitrogen of M22 exhibit similar rotation patterns and isotropic motions. We discuss these findings in the context of the formation of multiple populations.

Unified Astronomy Thesaurus concepts: Globular star clusters (656); Star clusters (1567); Stellar populations (1622); Stellar kinematics (1608)

1. Introduction

An increasing amount of research is providing evidence for the presence of two main classes of globular clusters (GCs; e.g., Marino et al. 2009, 2019; Milone et al. 2017). While stars in the majority of Type I Galactic GCs exhibit homogeneous abundances of heavy elements (e.g., Carretta et al. 2009), a small but significant number of anomalous clusters (Type II GCs) show internal variations in metallicity and in those elements that are associated to *s* processes (e.g., Yong & Grundahl 2008; Da Costa et al. 2009; Yong et al. 2014; Johnson et al. 2015; Marino et al. 2015, 2019).

Type II GCs exhibit distinctive photometric features, including multimodal subgiant branches (SGBs) in color–magnitude diagrams (CMDs) made with optical filters (e.g., Milone et al. 2008; Marino et al. 2009; Piotto et al. 2012), and multimodal red giant branches (RGBs) and SGBs in the *I* versus $U - I$ or *V* versus $U - V$ CMDs, with metal-rich stars populating red RGBs and faint SGBs (e.g., Marino et al. 2011; Lee 2015, 2020).

Based on multiband photometry of 58 GCs, Milone et al. (2017) find that Type II GCs make up 17% of the studied clusters. The fact that Type II clusters exhibit star-to-star metallicity variation suggests that they have been able to retain a small amount of the material ejected by supernovae. In this respect, they differ from Type I GCs, where supernova yields

seem to have no effect on the chemical composition of second-population stars.

Because of their high total masses and the complexity of their stellar populations, it has been suggested that Type II GCs formed in the environment of dwarf galaxies, e.g., in their nucleus.

These galaxies are then tidally destroyed by the interaction with the Milky Way. This possibility is supported by the observation that the Type II GC M54 lies in the nucleus of the Sagittarius dwarf galaxy (Bellazzini et al. 2008) and by the fact that the class of Type II GC includes NGC 5139 (ω Centauri), which is often considered the remnant of a dwarf (e.g., Bekki & Freeman 2003). Moreover, based on the integrals of motion of their orbits, at least half of the known Type II GCs (7 of 13 clusters) are associated with the Enceladus galaxy, thus demonstrating their extragalactic origin (Milone et al. 2020).

Remarkably, the evidence that both metal-rich and metal-poor stars of most Type II GCs host stellar populations with different light-element abundances (e.g., Marino et al. 2009, 2011) indicates that independent processes are responsible for the heavy-element enrichment and for the variation of light elements. Insights on the formation processes can be gained via the study of the kinematics of stellar populations with different chemical compositions.

Indeed, the various scenarios on the formation of multiple populations in GCs suggest that second-generation stars are

born in the cluster center, in a high-density subsystem embedded in a more extended first generation (D'Ercole et al. 2008; Calura et al. 2019, and references therein). *N*-body simulations (e.g., Mastrobuono-Battisti & Perets 2013, 2016; Vesperini et al. 2013; Hénault-Brunet et al. 2015; Tiongco et al. 2019) demonstrate that the dynamical evolution of second-generation stars should be significantly different from that of the first generation, and the signature of the different initial conditions could be detected in present-day GC kinematics of GCs where the stars are not fully mixed. Hence, the present-day dynamics of stellar populations with different metallicities and light-element abundances provide a unique window into the origin of multiple populations in Type II GCs.

In recent papers, we exploited Gaia Data Release 2 (DR2, Gaia Collaboration et al. 2018) proper motions to investigate the kinematics of stellar populations with different light-element abundances of Type I GCs (Milone et al. 2018; Cordoni et al. 2020). We find that multiple stellar populations of the GCs NGC 0288, NGC 6121, NGC 6752, and NGC 6838 share similar internal kinematics and morphology, in contrast with what is observed in NGC 104, NGC 5904, and NGC 6254. Indeed, when we select the main groups of N-poor and N-rich stars (called first and second population, respectively), we find that the two populations of NGC 104 share similar rotation patterns in the central region, and there are indications of different rotation in the cluster outskirts (Figure 10 in Cordoni et al. 2020). Moreover, N-rich stars of NGC 104 show stronger radial anisotropies than the first population (Milone et al. 2018; Cordoni et al. 2020, see their Figures 5 and 10, respectively). The rotation curves of N-poor and N-rich stars of NGC 5904 seem to exhibit different phases with a statistical significance of $\sim 2.5\sigma$ (Cordoni et al. 2020, see their Figure 8) and N-rich stars of NGC 5904 and exhibit higher ellipiticy than N-poor ones, in close analogy with what is observed in NGC 6254 (Cordoni et al. 2020, Figure 5 and 6).

Here, we extend the analysis to the Type II GCs ω Centauri and NGC 6656 (M22) to study the internal kinematics of stellar populations with different metallicities and light-element abundances. The main physical parameters of these two clusters, which share similar nucleosynthetic enrichment processes despite their different masses (e.g., Da Costa & Marino 2011), are listed in Table 2. In particular, we note that the long half-mass relaxation time of ω Centauri, which exceeds the Hubble time (Baumgardt & Hilker 2018), makes this cluster an ideal target for inferring the initial configuration of multiple stellar populations. In contrast, the half-mass relaxation time is shorter in M22 ($t_h \sim 3$ Gyr, e.g., Baumgardt & Hilker 2018).

The paper is organized as follows. In Section 2 we introduce the data set and describe the method with which we selected stars with high-precision proper motions. In Section 3 we identify multiple stellar populations in the CMDs. We discuss the properties of multiple populations with different iron content in Section 4, such as their spatial distributions, rotation, and velocity profiles. In Section 5 we extend the analysis to the stellar populations with different light-element abundances. Finally, the summary and discussion of the results are provided in Section 6.

2. Data and Data Analysis

To investigate the kinematics and the spatial distributions of stellar populations in M22 and ω Centauri, we combined the exquisite catalogs of proper motions and stellar positions provided by Gaia DR2 with multiband wide-field photometry from Stetson et al. (2019). Photometry and proper motions are available for stars of M22 and ω Centauri with radial distances smaller than $\sim 8'.4$ and $\sim 28'.5$ from the center, respectively. Most stars within $\sim 1'.7$ from the center of M22 and within $\sim 2'.5$ from the center of ω Centauri have poor-quality Gaia DR2 proper motions because of crowding. Hence, for the stars in these central regions, we used multiband photometry and relative proper motions from Hubble Space Telescope (HST) images.

Gaia DR2 proper motions are affected by systematic errors that depend on the positions and colors of the stars (e.g., Lindegren et al. 2018). We followed the method described by Vasiliev (2019), which accounts for systematic errors by enlarging the uncertainties associated with proper motion determinations. As a consequence, as discussed by Cordoni et al. (2020), the error bars provided in this work overestimate the true errors. Indeed, our main focus is the relative motion of the multiple stellar populations in ω Centauri and M22, which share similar colors in the Gaia passbands and at first approximation have similar spatial distributions. Hence, the effect of systematic errors on the relative motions of the distinct population may be partially canceling out. In the following, we provide details for the data from ground-based facilities and the HST.

2.1. Ground-based Data Set

We used the catalogs obtained by Stetson et al. (2019), which provide high-precision photometry of stars in the *U*, *B*, *V*, and *I* bands over a wide field of view. Details on the data set and on the data reduction are provided by Stetson (2005), Monelli et al. (2013), and Stetson et al. (2019). *U*-band photometry of M22 is taken from Marino et al. (2015) and was derived from images collected with the Wide Field Imager of the ESO/MPI telescope at the Cerro Tololo Inter-American Observatory (WFI at 2.2 m). We refer to Marino and collaborators for details on their photometric catalog. The photometry is calibrated on the photometric system by Landolt (1992).

Bellini et al. (2009) used multi-epoch data acquired by WFI at 2.2 m to derive proper motions of stars in the field of view of ω Centauri, which are suitable for separating field stars from cluster members. Due to crowding, stellar proper motions from GAIA DR2 are not available for most of the stars in the central region of ω Centauri. To increase the sample size, we identified the stars without Gaia DR2 proper motions those that according to Bellini et al. (2009) have membership probabilities higher than 90% and included these stars in the analysis of the spatial distribution of multiple stellar populations of ω Centauri.

We emphasize that proper motions from Bellini and collaborators are not included in our study on the kinematics of ω Centauri. Instead, as we discuss widely in the next sections, the internal kinematics of multiple stellar populations in ω Centauri and M22 are investigated using high-precision proper motions from HST images and from Gaia DR2 alone.

2.2. HST Data Set

HST photometry and relative proper motions are used to investigate stellar populations of M22 and ω Centauri with radial distances smaller than $\sim 1'.7$ and $\sim 2'.5$, respectively.

Table 1
Description of the HST Images Used in the Paper to Derive Stellar Proper Motions

Camera	Filter	Date	$N \times$ Exptime	Program	PI
			M22		
ACS/WFC	F606W	2006 Jul 1	$3\,s + 4 \times 55\,s$	10775	A. Sarajedini
ACS/WFC	F814W	2006 Jul 1	$3\,s + 4 \times 65\,s$	10775	A. Sarajedini
WFC3/UVIS	F814W	2010 Sep 23	$2 \times 50\,s$	12311	G. Piotto
WFC3/UVIS	F814W	2011 Mar 17–18	$2 \times 50\,s$	12311	G. Piotto
WFC3/UVIS	F395N	2011 May 18	$2 \times 631\,s + 2 \times 697\,s$	12193	J.-W. Lee
WFC3/UVIS	F467M	2011 May 18	$2 \times 361\,s + 2 \times 367\,s$	12193	J.-W. Lee
WFC3/UVIS	F547M	2011 May 18	$74\,s + 3 \times 75\,s$	12193	J.-W. Lee
WFC3/UVIS	F438W	2014 Jul 17	$2 \times 141\,s$	13297	G. Piotto
			ω Centauri		
ACS/WFC	F435W	2002 Jun 27	$12\,s + 3 \times 340\,s$	9442	A. Cool
WFC3/UVIS	F438W	2009 Jul 15	$35\,s$	11452	J. Kim Quijano
WFC3/UVIS	F814W	2009 Jul 15	$35\,s$	11452	J. Kim Quijano
WFC3/UVIS	F814W	2010 Jan 12	$8 \times 40\,s$	11911	E. Sabbi
WFC3/UVIS	F438W	2010 Jan 14	$9 \times 350\,s$	11911	E. Sabbi
WFC3/UVIS	F814W	2010 Jan 14	$40\,s$	11911	E. Sabbi
WFC3/UVIS	F438W	2010 Apr 29	$7 \times 350\,s$	11911	E. Sabbi
WFC3/UVIS	F814W	2010 Apr 29	$9 \times 40\,s$	11911	E. Sabbi
WFC3/UVIS	F438W	2010 Jun 30	$9 \times 350\,s$	11911	E. Sabbi
WFC3/UVIS	F814W	2010 Jun 30	$4 \times 40\,s$	11911	E. Sabbi
WFC3/UVIS	F438W	2010 Jul 04	$350\,s$	11911	E. Sabbi
WFC3/UVIS	F814W	2010 Jul 04	$5 \times 40\,s$	11911	E. Sabbi
WFC3/UVIS	F438W	2011 Feb 15	$350\,s$	12339	E. Sabbi
WFC3/UVIS	F438W	2011 Mar 24	$8 \times 350\,s$	12339	E. Sabbi
ACS/WFC	F435W	2012 Aug 18	$9 \times 6\,s + 9 \times 339\,s$	13066	L. J. Smith
ACS/WFC	F435W	2019 Aug 27	$42\,s + 3 \times 647\,s$	15594	V. Kozhurina-Platais

To identify the stellar populations along the RGB of M22 and ω Centauri, we used the catalogs by Milone et al. (2017, 2018), which include photometry collected through the F275W, F336W, F438W, and F814W bands of the Ultraviolet and Visual Channel of the Wide Field Camera 3 (UVIS/WFC3).

The main properties of the images that we used to derive relative stellar proper motions are summarized in Table 1. To derive the photometry and the astrometry of all the stars, we used the FORTRAN software package KS2 developed by Jay Anderson, (see, e.g., Anderson et al. 2008; Sabbi et al. 2016, for details). Because we are interested to determine the proper motion, we reduced the images collected in different epochs independently, and measured the position of stars at each epoch. Stellar positions have been corrected for geometrical distortion by using of the solutions provided by Bellini & Bedin (2009) and Bellini et al. (2011). We measured proper motions as in Piotto et al. (2012, see their Section 4) by comparing the distortion-corrected stellar positions at different epochs. To derive the proper motion of each star and minimize the effect of any residual distortion, we used the sample of 45 nearest cluster members as reference stars to fix the zero-point of the motion. Hence, our measurements from HST data provide proper motions relative to the average Local Cluster motion.

2.3. Selection of Cluster Members

To explore the internal kinematics of the stellar populations from Gaia DR2 data, we identified the sample of stars with accurate astrophotometric measurements following the method described in our previous papers (Cordoni et al. 2018, 2020; Milone et al. 2018). In a nutshell, we first selected only stars with accurate proper motion measurements by using both the

`astrometric_gof_al`(As_gof_al) and the renormalized unit weight error parameters (see Lindegren et al. 2018). We then selected cluster members from the proper motion vector-point diagram. We refer to Cordoni et al. (2020) for a detailed description of the procedure. Finally, we corrected the photometry of cluster members for differential reddening using the method in Milone et al. (2012, see their Section 3.1). The final CMDs are shown in the left panels of Figure 1.

In the case of the HST data set, the photometric catalogs by Milone et al. (2017, 2018) already distinguished cluster members and field stars based on stellar proper motions. Hence, we included in the analysis only those stars that according to Milone and collaborators belong to M22 and ω Centauri.

3. Multiple Populations in the CMDs

As shown in Marino et al. (2019), Type II GCs exhibit multimodal SGBs and RGBs in the photometric diagrams made with $U - V$ and $U - I$ colors that correspond to stellar populations with different metallicities. Hence, we exploit the I versus $U - I$ CMD of ω Centauri and the V versus $U - V$ CMD of M22 to separate the stellar populations with a low content of iron and s-process elements (Fe-poor) from the chemically enriched ones (Fe-rich).

The main procedure (I) for identifying Fe-poor and Fe-rich stars is similar to that used in Cordoni et al. (2020, see their Figure 2). Briefly, we determined the RGB boundaries as the 4th and 96th percentile of the color distributions, and we verticalized the CMD following the procedure described in Milone et al. (2017, see their Section 3). Finally, we derived the kernel-density distributions of stars in the verticalized I versus $\Delta(U - I)$ CMDs (red lines in the right panels of Figure 1) and
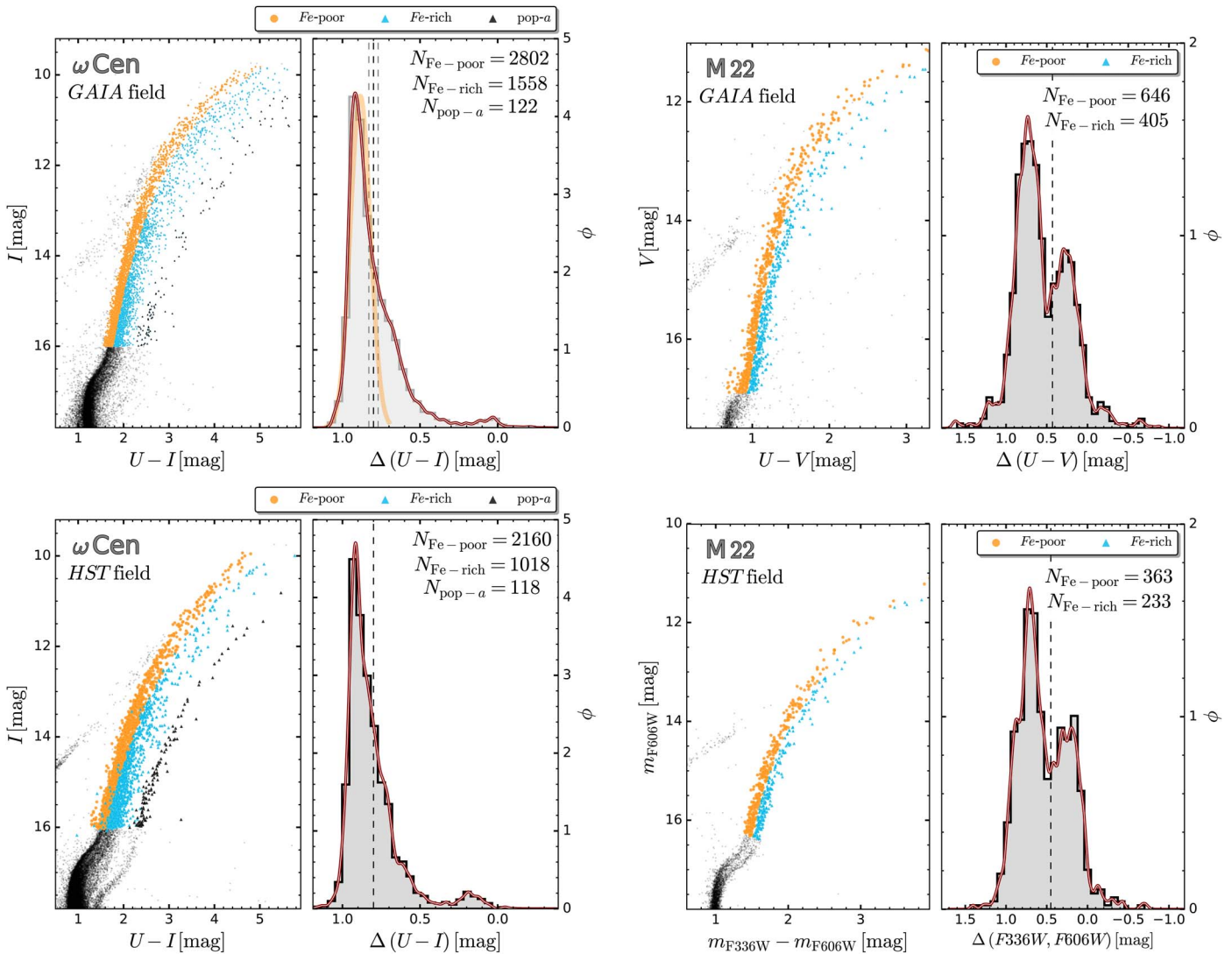
Figure 1. I vs. $U - I$ and V vs. $U - V$ diagrams for the selected cluster members of ω Centauri (upper left) and M22 (upper right) from ground-based photometry (upper panels). We also show the histogram and the kernel-density distributions of $\Delta(U - I)$ and $\Delta(U - V)$ for the selected RGB stars of ω Centauri and M22. The vertical dashed black lines are used to select Fe-poor and Fe-rich stars in procedure I, marked with orange circles and cyan triangles, respectively. The orange Gaussian and the dashed gray lines in the top left panels are adopted to identify alternative groups of stars with different metallicities of ω Centauri from procedures II and III. See text for details. The lower panels show the corresponding diagrams from HST photometry of stars in the internal fields. To ensure consistency between the selection of Fe-poor and Fe-rich stars in the two fields of ω Centauri, we converted HST magnitudes m_{F336W} and m_{F814W} into U and I magnitudes of the photometric system by Landolt (1992).

identified by eye the groups of Fe-poor (orange dots) and Fe-rich (cyan triangles) RGB stars, which are located on the left and right side of the vertical dashed line, respectively. In the case of ω Centauri, we adopted an intermediate step before we identified Fe-poor and Fe-rich stars in the HST inner field. Specifically, to ensure consistency between the two fields and data sets, we converted the m_{F336W} and m_{F814W} magnitudes into U and I magnitudes. The same process was redundant in the simpler case of M22, as revealed by the right panels of Figure 1.

To verify the effect of the adopted selection of ω Centauri stars with different metallicities on the conclusions of the paper, we adopted two additional procedures (II and III). Procedure II consists of excluding stars with $U - I$ colors within ± 0.03 mag from the vertical dashed line from the metal-poor and metal-rich sample defined above. Procedure III is based on the Monte Carlo method for selection of metal-rich and metal-poor stars. We fit the $\Delta(U - I)$ distributions of stars

with $\Delta(U - I) > 0.85$ with a Gaussian function by means of least squares (transparent orange line in the top left panel of Figure 1). Then, we randomly associated each star with a probability to belong to the metal-poor and metal-rich sample based on ratio between the value of the best-fit Gaussian and the histogram distribution corresponding to its $\Delta(U - I)$ value. In the following, we present results based on the selection from procedure I, while in Section 6 we compare the results from the procedures I, II, and III to demonstrate that the conclusions of the paper do not depend on the selection criterion.

3.1. Multiple Populations with Different Light-element Abundances in ω Centauri

Work based on high-resolution spectroscopy reveals that stellar groups in different metallicity bins of ω Centauri host subpopulations with different light-element abundances (e.g., Johnson & Pilachowski 2010; Marino et al. 2010, 2011).
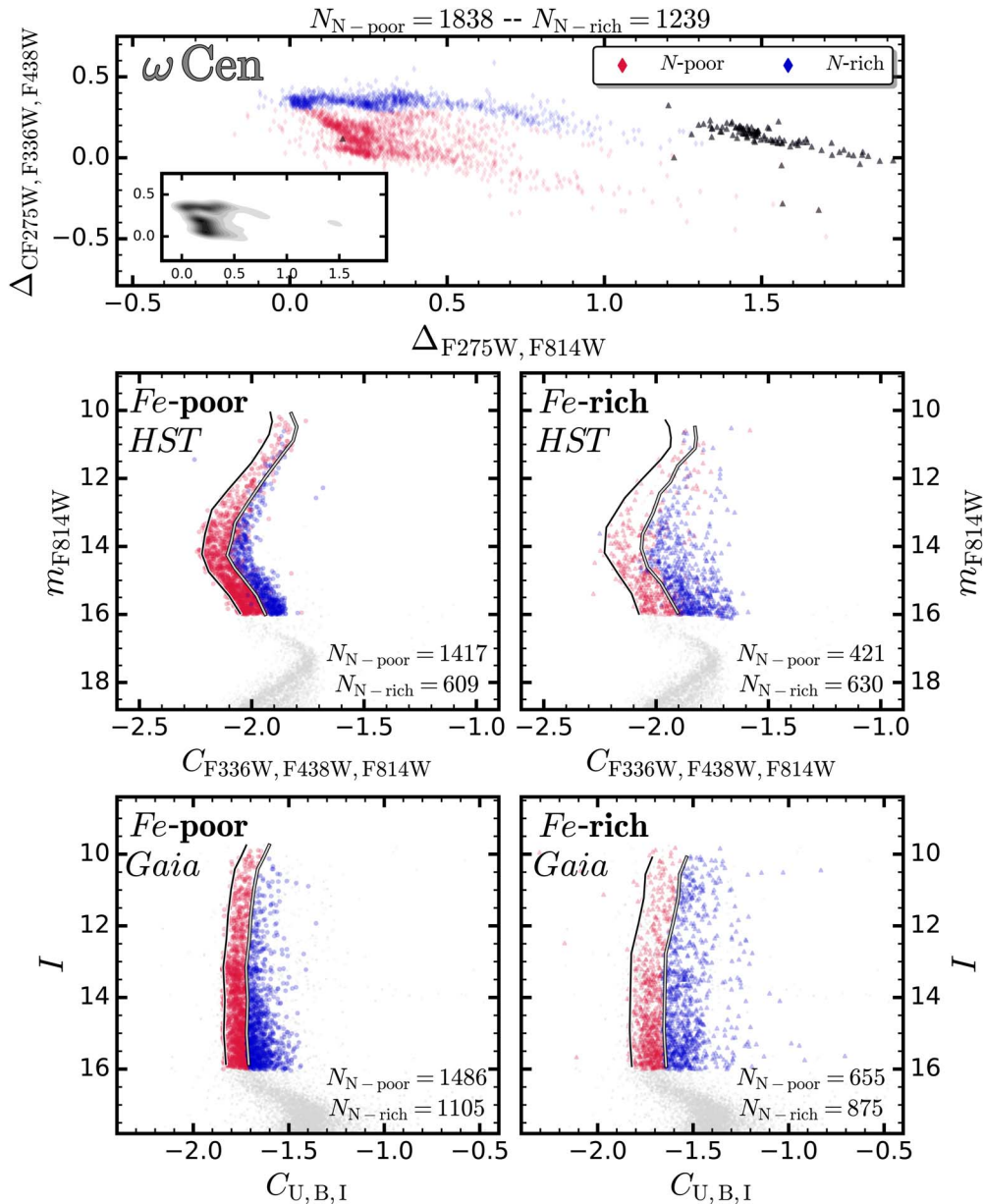
Figure 2. Top panel: pseudo-two-color diagram, i.e., the ChM of ω Centauri. We adopted the selection criteria of Marino et al. (2019) to identify stars with different nitrogen abundances. Specifically, N-poor stars (lower and middle stream) are represented with red diamonds, while N-rich stars (upper stream) are marked with blue diamonds. pop-a stars are marked with solid black triangles. The bottom left inset shows the 2D-KDE of the same ChM. Middle panels: m_{F814W} vs. $C_{F336W,F438W,F814W}$ for Fe-poor (left) and Fe-rich (right) stars as selected in Section 3. The fiducial lines in the CMDs are derived with the purpose of distinguishing stellar populations with different nitrogen abundances among stars with different iron. Lower panels: I vs. $C_{U,B,I}$ again for metal-poor (left) and metal-rich stars (right). The separation into N-poor and N-rich stars is derived by shifting the bluest RGBs from the quantity derived in the HST CMDs, as discussed in Section 5.

An efficient tool to distinguish the distinct populations in GCs is provided by the pseudo-two-color diagram called chromosome map, which revealed that ω Centauri hosts at least 16 subpopulations (ChM, Milone et al. 2015, 2017). Based on multiband HST photometry of ω Centauri, Marino et al. (2019) identified three main groups of stars that define distinct streams in the ChM. The stars of each stream span similar intervals of [Fe/H] but have a different content of He, C, N, O, and Na. Specifically, the upper stream is composed of stars with extreme nitrogen abundances (hereafter N-rich sample), while middle- and lower-stream stars have low and intermediate [N/Fe], respectively, and are called N-poor sample in the following. N-rich and N-poor stars are represented with blue

and red points, respectively, in the chromosome map of ω Centauri plotted in the upper panel of Figure 2.

Unfortunately, the HST photometry that is required to build the ChM is only available for stars with radial distances smaller than $\sim 2'.5$. Hence, alternative photometric diagrams are needed to distinguish N-rich and N-poor stars in the external region of ω Centauri.

As shown in the middle panels of Figure 2, Fe-rich and Fe-poor stellar populations with different nitrogen abundances also populate different RGB regions in the m_{F814W} versus $C_{F336W,F438W,F814W} = (m_{F336W} - m_{F438W}) - (m_{F438W} - m_{F814W})$ pseudo-CMD. Specifically, N-poor stars exhibit lower $C_{F336W,F438W,F814W}$ values than N-rich stars with the same luminosity.

The lower panels of Figure 2 show the I versus $C_{U,B,I} = (U - B) - (B - I)$ pseudo-CMD for stars with radial distances larger than $\sim 2'\!.5$ from ground-based photometry. Because the F336W, F438W, and F814W filters are the HST-analogs of U, B, and I, the $C_{F336W,F438W,F814W}$ and $C_{U,B,I}$ have similar sensitivity to stellar populations with different chemical composition. We exploited HST photometry to distinguish stellar populations with different nitrogen abundances, and then translated the separation into ground-based photometry.

The solid black lines superimposed on the m_{F814W} versus $C_{F336W,F438W,F814W}$ and the I versus $C_{U,B,I}$ diagrams are derived as in Section 2.3 and mark the bluest boundary of the RGBs. We determined the gray lines in the m_{F814W} versus $C_{F336W,F438W,F814W}$ diagrams with the criteria to separate most of N-poor stars from N-rich stars, as selected in the ChM shown in the top panel.

To separate the bulk of N-rich and N-poor stars in the ground-based CMD, we first estimated the $C_{F336W,F438W,F814W}$ distance between the gray and black fiducials of each CMD for stars with different luminosities ($\Delta C_{F336W,F438W,F814W}$). We then determined the bluest RGB boundaries in the I versus $C_{U,B,I}$ for both Fe-poor and Fe-rich stars (lower panels). Finally, we shifted these fiducial lines by a certain amount, $\Delta C_{U,B,I}$, that corresponds to the $\Delta C_{F336W,F438W,F814W}$ quantity derived from HST photometry.

The selected N-poor and N-rich stars are shown with red and blue circles and triangles, respectively, for the metal-poor and metal-rich stars.

ω Centauri hosts a sample of metal-rich stars ([Fe/H] $\gtrsim -0.9$) that are called population-a stars and define a distinct RGB sequence on the red side of the bulk of RGB stars (e.g., Lee et al. 1999; Pancino et al. 2000). In the left panels of Figure 1 we identify population-a stars in the I versus $U - I$ (lower left panel) and I versus $U - I$ CMDs (lower right panel). The position of population-a stars in the ChM (see the upper panel of Figure 2) corroborate previous conclusion by Marino et al. (2011, 2019) that the majority of population-a stars belongs to the N-rich sample, and a small group of population-a stars are N-poor. Specifically, $\sim 92\%$ of population-a stars are enhanced in nitrogen, while only $\sim 8\%$ are N-poor.

We find that all the aforementioned stellar populations exhibit average proper motions consistent with each other within 1σ.

4. Kinematics of Stellar Populations with Different Metallicities

4.1. Spatial Distribution of Multiple Populations

In the following, we extend the procedure to the sample of Fe-poor and Fe-rich stars of ω Centauri and M22 that is based on the two-dimensional binned kernel-density estimate (Wand 2015) used by Cordoni et al. (2020) to analyze the spatial distributions of stellar populations in seven Type I GCs.

Because of crowding, stellar proper motions from GAIA DR2 are not available for most of the stars in the central regions of ω Centauri. To increase the number of studied stars of ω Centauri cluster members, we included in the analysis stars whose membership probabilities are higher than 90% according to Bellini et al. (2009).

The results for ω Centauri are illustrated in the upper panels of Figure 3, where we show the density plots of the Fe-poor
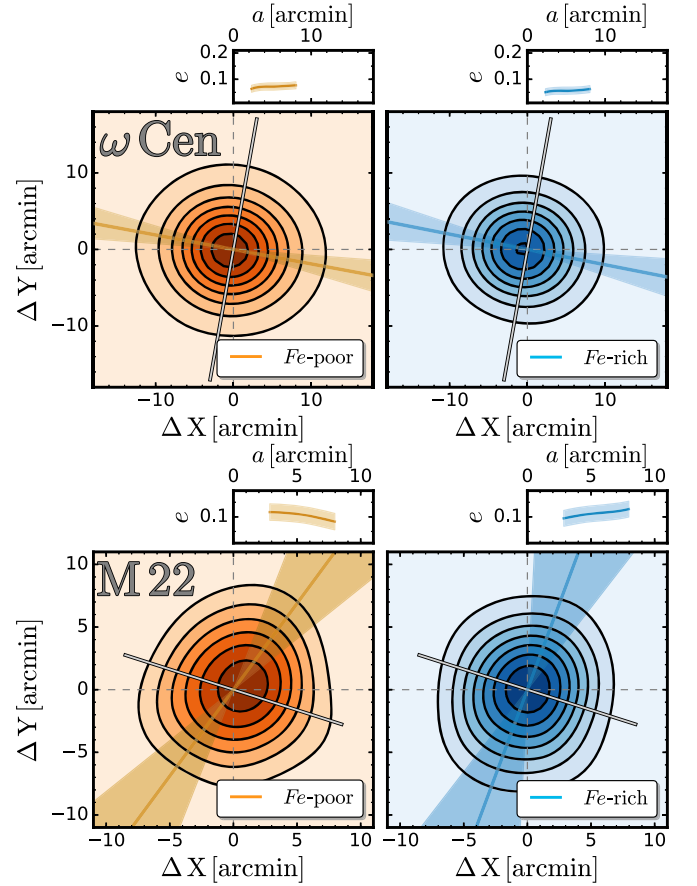

Figure 3. Density maps of metal-rich and metal-poor populations in ω Centauri (top panels) and M22 (bottom panels). The quantities on the abscissa and ordinate are the projected stellar coordinates relative to the cluster center. The color levels are indicative of stellar density and are based on the 2D binned kernel-density estimate (Wand 2015). The iso(density contours are shown in each panel together with the rotation axis as determined in Sollima et al. (2019) solid black-gray line). Red and blue lines in the top insets show the ellipticity against the major axis, while the shaded regions represent the 1σ confidence bands.

(left) and Fe-rich (right) stars in orange and blue, respectively. The contours are determined by smoothing the data points with a Gaussian kernel of fixed size. The size is chosen with the criterion of minimizing the small-scale structure without loosing the information on the global spatial distribution. To properly compare the results, we adopted the same kernel size for all the populations of both clusters.

We calculated six isodensity contours for each population and used the least-squares method to fit each contour with an ellipse as in Halır and Flusser (1998). The directions of the resulting minor and major axes are plotted in each panel. The resulting ellipticity, e, is plotted as a function of the semimajor axis, a, in Figure 4.

We confirm that ω Centauri has an elliptical shape (e.g., Harris 1996).

The ellipticity of Fe-poor and Fe-rich stars slightly increases from $e \sim 0.05$ to 0.07 and from $e \sim 0.06$ to 0.08, respectively, when we move from $a \sim 3'$ to $15'$. As a consequence, the ellipticity difference is $\Delta e \sim 0.015$ with a statistical significance of $\sim 70\%$.

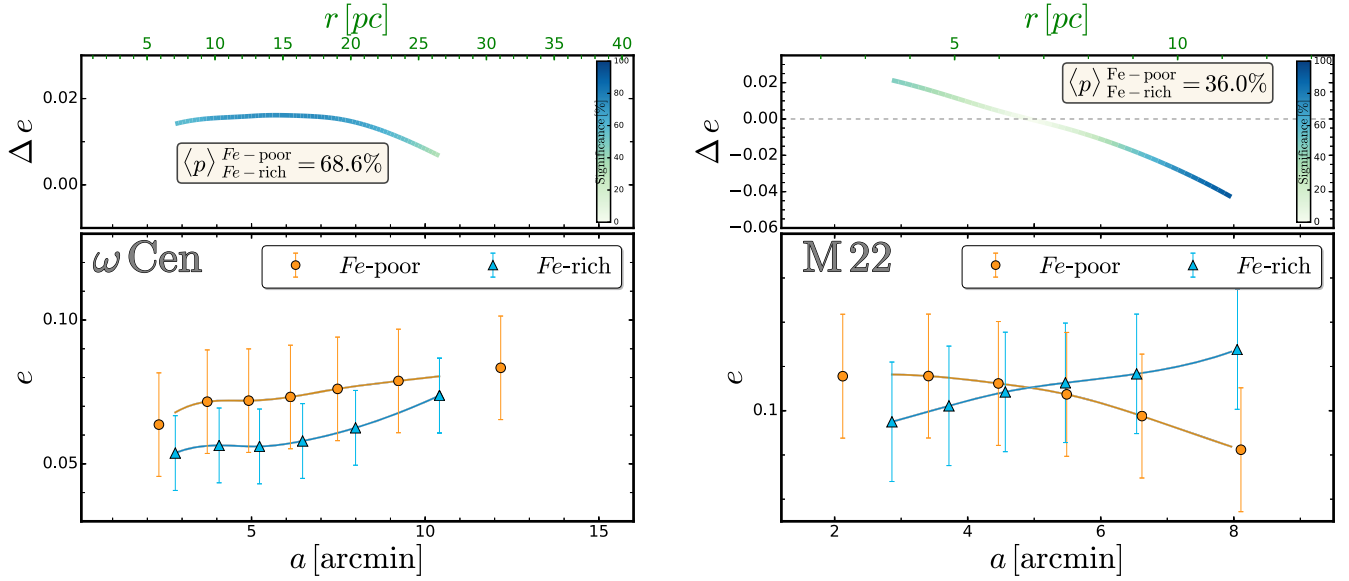The major axis of the best-fit ellipses are coincident within one sigma in both populations.

Figure 4. Ellipticity, e, of ellipses that best fit the spatial distribution of the different stellar populations of ω Centauri (left) and M22 (right) against the semimajor axis, a (lower panels). The upper panels show the difference between the ellipticity profiles as a function of a. The color level indicates the statistical significance of the difference, as indicated by the color bar. See text for details.

Table 2
Identification, Positional Data, and Adopted Structural Parameters for the Analyzed Type-II Clusters

ID	R.A. (J2000)[a]	Decl. (J2000)[a]	Mass[b] ($M_\odot$)	$d_{\rm Sun}$[b] (kpc)	$R_{\rm Gal}$[a] (kpc)	$R_{\rm c}$[b] (kpc)	$R_{\rm h}$[b] (arcmin)	$R_{\rm t}$[a] (arcmin)	$\log t_{\rm h}$[b] (yr)	$\bar{V}_{\rm LoS}$[b] (km s^{-1})
ω Centauri	13 26 47.24	-47 28 46.5	3.36×10^6	5.2	6.40	2.37	5.00	48.4	10.39	234.28
M22	18 36 23.94	-23 54 17.1	4.16×10^5	3.2	4.90	1.33	3.36	31.9	9.45	-147.76

Notes. For each cluster we list position (R.A., decl.), mass, distance from the Sun, galactocentric radius ($R_{\rm Gal}$), core radius ($R_{\rm c}$), half-light radius ($R_{\rm h}$), tidal radius ($R_{\rm t}$), logarithm of the half-mass relaxation time ($t_{\rm h}$), and line-of-sight mean velocity ($\bar{V}_{\rm LoS}$).
[a] From Harris (1996, updated as in 2010).
[b] From Baumgardt & Hilker (2018).

In the case of M22, both Fe-poor and Fe-rich stars have similar ellipticities ($e \simeq 0.1$) over the entire analyzed field of view, and their major axis have similar directions.

Finally, as expected for oblate rotators, we find that the rotation axis (from Sollima et al. 2019, solid black-gray line in Figure 3) is coincident with the semiminor axis of the best-fit ellipses, i.e., perpendicular to the semimajor axis plotted in Figure 3.

4.2. Rotation in the Plane of the Sky

4.2.1. Rotation Profile

In this subsection, we analyze the average internal motions of Fe-poor and Fe-rich stars as a function of the radial distance from the cluster center. As a first step, we converted the $\mu_\alpha \cos\delta$ and μ_δ components of proper motions into a radial ($\mu_{\rm RAD}$) and a tangential ($\mu_{\rm TAN}$) motion on the plane of the sky, correcting for the effect of perspective expansion/contraction as in van de Ven et al. (2006). We divided the cluster fields of ω Centauri and M22 into 17 and 6 circular annulii, respectively, determined with the naive estimator method (Silverman 1986). To account for the different stellar densities at different distances from the cluster center, we used wider bins in the outskirts of the cluster (in the case of ω Centauri: 5′ for the innermost bin, 3′3 for $1.2R_{\rm h} < r < 3.2R_{\rm h}$, and 4′2 for $3.2R_{\rm h} < r < 4.2R_{\rm h}$ and 5′9 for $r > 4.2R_{\rm h}$).

For each annulus, we used the routines provided by Vasiliev (2019) to compute the median radial ($\Delta\mu_{\rm RAD}$) and tangential ($\Delta\mu_{\rm TAN}$) motions, thus accounting for systematic errors in Gaia DR2 proper motions. Furthermore, Gaia DR2 uncertainties on proper motion are underestimated by a factor of $\sim 10\%$ and $\sim 30\%$ for stars with magnitude $G > 16$ and $G < 13$, respectively.

We therefore artificially increased the observed uncertainties on the proper motions as in Bianchini et al. (2019) .

We then estimated the uncertainty relative to each point by bootstrapping with replacements, which we performed 1000 times.

The radial and tangential proper motions have been converted from mas yr^{-1} into km s^{-1}, ($\Delta V_{\rm RAD}$ and $\Delta V_{\rm TAN}$) by adopting the distances listed in Table 2 that were derived in Baumgardt & Hilker (2018). The radial and tangential velocity versus the distance from the cluster center is shown in Figure 5. The radial coordinate has been normalized to the half-light radius from Baumgardt & Hilker 2018 (see Table 2). A visual inspection of Figure 5 reveals that the radial profiles of ω Centauri and M22 are consistent with a zero-velocity up to at least ~ 4 and ~ 2 $R_{\rm h}$, respectively. A possible exception is provided by the Fe-rich population of ω Centauri, which seems to exhibit higher radial velocities for distances greater than $4 R_{\rm h}$.

Concerning the tangential profiles, we find positive values of $\Delta V_{\rm TAN}$ over the entire analyzed radial interval, thus favoring
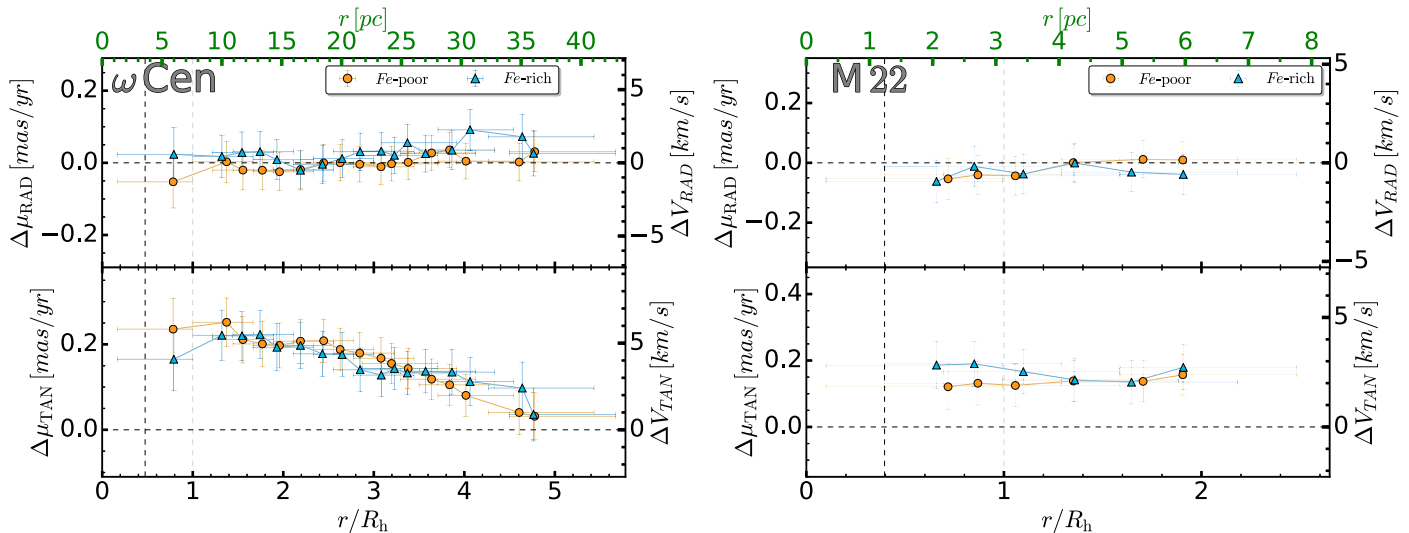
Figure 5. Average radial and tangential profile as a function of the radial distance from the cluster centers for ω Centauri (left) and M22 (right). The radial quantity is normalized over the half-light radius from Baumgardt & Hilker (2018). Orange circles and cyan triangles represent Fe-poor and Fe-rich stars, respectively.

rotation among all the studied populations of ω Centauri and M22. The tangential profiles of Fe-poor and Fe-rich stars in ω Centauri exhibit their maximum amplitudes of about 6 km s^{-1} at radial distances of about one half-light radii and steadily decrease toward larger distances from the cluster center. In the case of M22, both populations are consistent with a flat tangential profile in the analyzed radial interval. Our data do not allow us to determine whether the rotation pattern of M22 strongly differs from that of ω Centauri, or if the apparently flat rotation of M22 is due to the lack of observations in the external regions.

To compare the average velocity profiles of stellar populations, we used the same procedure as described in Cordoni et al. (2020, see their Section 5). We first used the Anderson–Darling (A-D) test to estimate the probability, p, that the tangential and radial motions of Fe-poor and Fe-rich stars are drawn from the same parent population. Furthermore, we compared the observed velocity profiles of Fe-poor and Fe-rich stars with $N_{sim} = 1000$ velocity profiles of simulated Fe-poor and Fe-rich stars. We assumed that the simulated stellar populations share the same velocity profiles and exhibit the same errors as the observed stars. For each bin we calculated the observed difference and counted the number of simulations that resulted in a difference greater than observed.

The fraction of simulations, $N*/N_{sim}$, where $\Delta_{chi} \geqslant \Delta_{obs}$ is indicative of the significance of the difference of the observed profiles. To quantify the global significance, we computed the median of the significance of each bin, as well as the maximum and minimum values along the observed profiles. The results are listed in Table 3 for each pair of velocity profiles.

The results from the A-D test and the values of N_{sim} are listed in Table 3 and reveal that we find no differences between the observed velocity profiles of Fe-poor and Fe-rich stars in ω Centauri or in M22.

4.2.2. Global Rotation

To further quantify the rotation in the plane of the sky of both clusters, we adopted the procedure described in Cordoni et al. (2020, see their Section 3).

Briefly, we divided the field of view of each cluster into 30 circular sectors with an arc length of 45°. We computed the median $\mu_\alpha \cos \delta$ and μ_δ motions for Fe-poor and Fe-rich stars in each sector, and then subtracted the cluster median motion. As previously done for the radial and tangential velocity profiles, we accounted for Gaia systematic errors as in Vasiliev (2019).

The resulting quantities, $\Delta\mu_\alpha \cos \delta$ and $\Delta\mu_\delta$, are shown in the bottom panels of Figure 6 as a function of the position angle θ, defined counterclockwise from the east. A visual inspection of this figure suggests that consistently with the previous method, both populations of ω Centauri and M22 rotate in the plane of the sky. This result is illustrated in the top panels of Figure 6, where we show the positions of the stars relative to the cluster center, together with the vectors that indicate the median motions of Fe-poor and Fe-rich stars computed in each circular sector.

As in Cordoni et al. (2020), we used the least-squares technique to fit the sine function

$$f(\theta) = M + A \cdot \sin(F \cdot \theta + \phi) \tag{1}$$

to all Fe-poor and Fe-rich stars in ω Centauri and M22. The best-fit functions to Fe-poor and Fe-rich stars are represented with orange and azure lines, respectively, in the bottom panels of Figure 6. We estimate the goodness-of-fit by means of the r^2 parameter:

$$r^2 = 1 - \frac{\sum_i (y_i - f(\theta, i))^2}{\sum_i (f(\theta, i) - \bar{y})^2}, \tag{2}$$

where y_i is the value of $\mu_\alpha \cos \delta (\mu_\delta)$ for each star, i, θ is the corresponding position angle, $\bar{y}$ is the average value of y, and f is the best-fit function. The r^2 values for Fe-poor and Fe-rich are listed in bottom left insets of Figure 6. The fact that the motions of ω Centauri and M22 provide a good match between the data and the sine interpolation ($r^2 > 0.7$) confirms the visual impression that both populations rotate in the plane of the sky.

Figure 6 shows that the sine functions that provide the best fit of Fe-poor and Fe-rich stars exhibit slightly different rotation

Table 3
Comparison of the Rotation Curves in the $\mu_\alpha \cos\delta$ versus θ, μ_δ versus θ versus θ Planes of Metal-Poor and Metal-Rich Stars in the Entire Field of View of M22 and ω Centauri and in the Analyzed Three Subregions, R_1, R_2, and R_3 of the ω Centauri Field of View

ID		Region	Motion Component	$\Delta A^{\rm obs}$ (mas yr^{-1})	$\Delta \phi^{\rm obs}$ (rad)	$P(|\Delta A^{\rm sim}| \geqslant |\Delta A^{\rm obs}|)$	$P(|\Delta \phi^{\rm sim}| \geqslant |\Delta \phi^{\rm obs}|)$
ω Centauri	Fe-poor−Fe-rich	all	$\mu_\alpha \cos\delta$	0.006 ± 0.020	0.179 ± 0.090	0.756	0.403
			μ_δ	0.019 ± 0.022	0.192 ± 0.103	0.333	0.145
		R_1	$\mu_\alpha \cos\delta$	0.026 ± 0.038	0.113 ± 0.134	0.501	0.507
			μ_δ	0.055 ± 0.039	0.047 ± 0.125	0.193	0.845
		R_2	$\mu_\alpha \cos\delta$	0.006 ± 0.026	0.010 ± 0.121	0.848	0.941
			μ_δ	0.032 ± 0.028	0.261 ± 0.133	0.312	0.176
		R_3	$\mu_\alpha \cos\delta$	0.004 ± 0.026	0.399 ± 0.121	0.899	0.112
			μ_δ	0.004 ± 0.028	0.203 ± 0.129	0.916	0.454
	N-poor−N-rich	all	$\mu_\alpha \cos\delta$	0.044 ± 0.019	0.031 ± 0.092	0.878	0.795
			μ_δ	0.004 ± 0.018	0.051 ± 0.110	0.898	0.741
Fe-poor	N-poor−N-rich	all	$\mu_\alpha \cos\delta$	0.008 ± 0.023	0.038 ± 0.155	0.986	0.733
			μ_δ	0.015 ± 0.025	0.114 ± 0.180	0.541	0.147
Fe-rich	N-poor−N-rich	all	$\mu_\alpha \cos\delta$	0.023 ± 0.025	0.107 ± 0.101	0.538	0.655
			μ_δ	0.041 ± 0.024	0.112 ± 0.140	0.196	0.670
		R_1	$\mu_\alpha \cos\delta$	0.102 ± 0.035	0.111 ± 0.168	0.004	0.585
			μ_δ	0.093 ± 0.042	0.127 ± 0.118	0.009	0.477
		R_2	$\mu_\alpha \cos\delta$	0.030 ± 0.025	0.164 ± 0.186	0.451	0.569
			μ_δ	0.043 ± 0.024	0.067 ± 0.195	0.233	0.854
M22	Fe-poor−Fe-rich	all	$\mu_\alpha \cos\delta$	0.041 ± 0.020	0.210 ± 0.195	0.345	0.379
			μ_δ	0.014 ± 0.018	0.219 ± 0.224	0.745	0.231
	N-poor−N-rich	all	$\mu_\alpha \cos\delta$	0.067 ± 0.020	0.273 ± 0.153	0.077	0.396
			μ_δ	0.041 ± 0.022	0.024 ± 0.143	0.344	0.930

Note. We provide the A-D values from the A-D test and the corresponding probability that metal-poor and metal-rich stars come from the same parent distribution (*p*-val). We list the amplitude ($\Delta A^{\rm obs}$) and phase differences ($\Delta \phi^{\rm obs}$) of the curves that provide the best fit with metal-poor and metal-rich stars and the probability that the observed difference in phase and amplitude are due to observational errors as inferred from Monte Carlo simulations.

patterns. To investigate whether these differences are significant, we followed the procedure introduced by Cordoni et al. (2020, see their Section 4.1). Specifically, we ran 1000 Monte Carlo simulations of Fe-poor and Fe-rich stars where we assumed that the two populations exhibit the same proper motion distribution corresponding to the sine function that best fits the observed Fe-poor stars. We assumed that the two populations host the same number of stars as the observed Fe-rich and Fe-poor stars and added the corresponding observational errors to the simulated proper motions of each star. We used Equation (2) to fit the proper motion distributions of Fe-poor and Fe-rich stars and calculated the difference between their phases ($\Delta \phi^{\rm abs}$) and amplitudes ($\Delta A^{\rm abs}$). The number of simulations where ($|\Delta A^{\rm sim}| \geqslant |\Delta A^{\rm obs}|$) and ($|\Delta \phi^{\rm sim}| \geqslant |\Delta \phi^{\rm obs}|$) are indicative of the probability that the observed phase and amplitude differences between the corresponding rotation curves is due to observational errors alone. Results are listed in Table 3 and show that there is no evidence for significant differences between the amplitudes and phases of the sine functions that best matches the proper motion distributions of Fe-poor and Fe-rich stars of ω Centauri and M22.

For completeness, we plot in Figure 6 the values of $\mu_\alpha \cos\delta$ and μ_δ inferred for population-*a* stars against θ. The small sample of population-*a* stars does not allow us to properly fit the data with a sine function ($r^2 = 0.35$) and to understand whether this population shares the same rotation pattern as the bulk of ω Centauri stars.

4.2.3. Rotation of Stellar Populations in ω Centauri as a Function of Radial Distance

The large number of stars available in ω Centauri, together with the wide field of view of the Gaia DR2 and *UBI* ground-based photometry from Stetson et al. (2019), offers us the opportunity of investigating the rotation of Fe-poor and Fe-rich stars at different radial distances from the cluster center. We therefore exploit the median tangential velocity profile, which we reproposed in the top panel of Figure 7 to select three circular annuli (R_1–R_3 in Figure 7) with significantly different values of $\Delta \mu_{\rm TAN}$. The three regions are selected so that they contain a similar number of stars. The individual numbers of Fe-poor and Fe-rich stars is indicated in the insets of the lower panels of Figure 7.

We would like to point out that the ratio between Fe-poor and Fe-rich stars increases from the innermost region to the middle region, and remains almost constant between the middle and the outermost region. This confirms previous findings by Bellini et al. (2009).

Concerning the rotation in the plane of the sky, we find that the amplitudes of the best-fit sinusoidal functions for both Fe-poor and Fe-rich populations decrease from about 6 to 3 km s^{-1} when we move from $r \sim 1\,R_{\rm h}$ to $r \sim 4\,R_{\rm h}$.

The sine functions that provide the least-squares best fit with the observed proper motion distributions of Fe-poor and Fe-rich stars have slightly different values of amplitude A and phase ϕ. We followed the procedure introduced by Cordoni et al. (2020, see their Section 4.1) and described above to quantify the
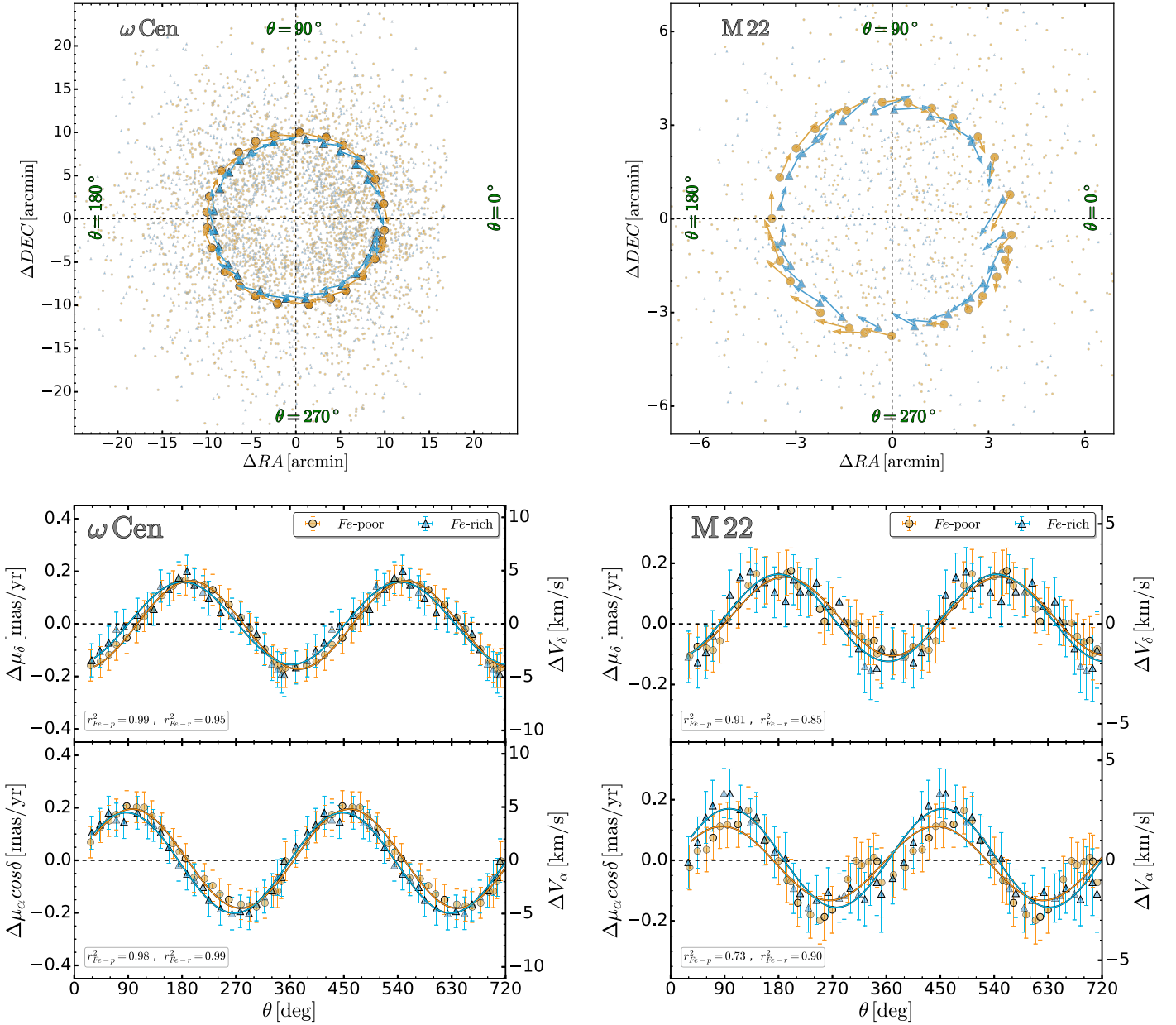
Figure 6. Top panels: relative positions of Fe-poor and Fe-rich RGB stars in ω Centauri and M22 with respect to the cluster center. Orange and cyan arrows indicate the average motion computed in each circular sector, as described in Section 4.2, scaled by a factor of 5 for clarity. The radial distances of the arrows correspond to the median radius of stars in each population. Bottom panels: $\Delta\mu_\alpha \cos\delta$ and $\Delta\mu_\delta$ as a function of θ for the two analyzed clusters. The bottom left insets show the value of the r^2 parameter, which is indicative of the quality of the fit.

statistical significance of the observed phase and amplitude differences. Results are listed in Table 3 and show that Fe-poor and Fe-rich stars are consistent with sharing the same rotation pattern in the three analyzed regions.

4.3. Velocity-dispersion Profiles

To estimate the radial and tangential velocity-dispersion profiles of Fe-poor and Fe-rich stars of ω Centauri and M22, we followed the procedure described in Mackey et al. (2013), Marino et al. (2014), and Bianchini et al. (2018). Briefly, we maximized the likelihood function

$$\lambda = \prod_{i=1}^{N} p(v_i, \epsilon_i)$$

with the probability of finding a star with velocity v_i and uncertainty ϵ_i defined by Equation (3). The corresponding uncertainties have been computed by bootstrapping with the replacement 1000 times,

$$p(v_i, \epsilon) = \frac{1}{2\pi\sqrt{(\sigma^2 + \epsilon_i^2)}} \exp\left(-\frac{(v_i - v)^2}{2(\sigma^2 + \epsilon_i^2)}\right). \qquad (3)$$

The radial and tangential velocity-dispersion profiles as a function of the radial distance from the cluster center are plotted in the upper panels of Figure 8, where we used filled and open symbols to represent results from Gaia DR2 and HST proper motions, respectively.

The velocity dispersions of ω Centauri and M22 reach their maximum values of $\sim$18 km s^{-1} and $\sim$9 km s^{-1}, respectively,
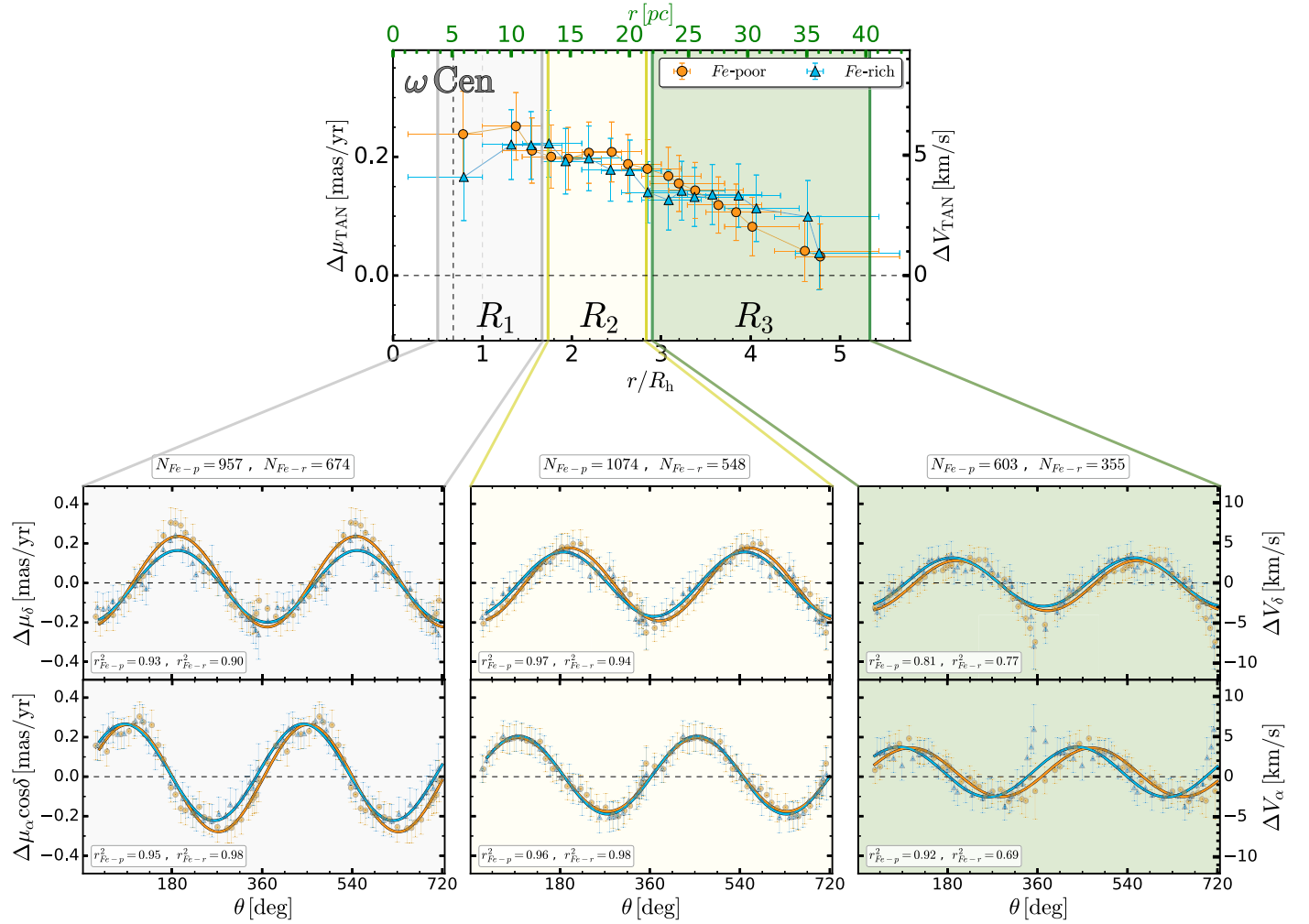
Figure 7. Top panel: reproduction of the $\Delta\mu_{\rm TAN}$ vs. $r/R_{\rm h}$ diagram of Fe-poor and Fe-rich stars in ω Centauri plotted in Figure 5. Bottom panels: $\Delta\mu_\alpha \cos\delta$ and $\Delta\mu_\delta$ against the position angle θ for stars in regions R_1–R_3 defined in the upper panel. The sine functions that provide the best fit with the observations of Fe-poor and Fe-rich stars are represented with orange and azure lines, respectively.

in the innermost analyzed regions and decline to ~7 and ~6 km s^{-1}, respectively, in the cluster outskirts.

We quantified the anisotropy of cluster stars as $\beta = \sigma_{\rm TAN}/\sigma_{\rm RAD} - 1$, with $\beta < 0$ indicating radial anisotropy and $\beta > 0$ tangential anisotropy. $\beta = 0$ is characteristic of an isotropic stellar system.

β is plotted as a function of the radial distance from the cluster center in the bottom panels of Figure 8. Finally, we assessed the statistical significance of the observed differences in the kinematical profiles with the same procedure as described in Cordoni et al. (2020). The average p-value, together with the its maximum and minimum, is listed in Table 4 for all the analyzed populations and subpopulations.

Our results show that the studied populations of ω Centauri are radially anisotropic in the central regions, with the Fe-rich population being more radially anisotropic than the Fe-poor populations. In the outermost region of the cluster, both populations are consistent with an isotropic system. Furthermore, the p-values listed in Table 4 show that the observed differences are statistically not significant.

In M22 the radial profiles of β for Fe-poor and Fe-rich stars are consistent with each other and are both approximately isotropic.

5. Multiple Stellar Populations with Different Light-element Abundances

In this section, we investigate the stellar populations of ω Centauri and M22 selected on the basis of their content of light elements. In ω Centauri, we analyzed the entire groups of N-rich and N-poor stars identified in Figure 2. Moreover, we separately compared the spatial distributions and the kinematics of the subsample of N-poor and N-rich stars that belong to the Fe-poor population alone and of the subsample of N-poor, N-rich and population-*a* stars among Fe-rich stars. In M22, which has a smaller number of RGB stars than ω Centauri, we limited the analysis to entire sample of N-rich and N-poor stars. The spatial distributions of the stellar populations with different light-elements of both M22 and ω Centauri are analyzed in Section 5.1, while Section 5.2 is focused on their internal kinematics.

5.1. Spatial Distribution of N-rich and N-poor Populations

To investigate the spatial distributions of stellar populations with different nitrogen content, we extended the analysis introduced in Sections 4.1 to the selected groups of N-rich and
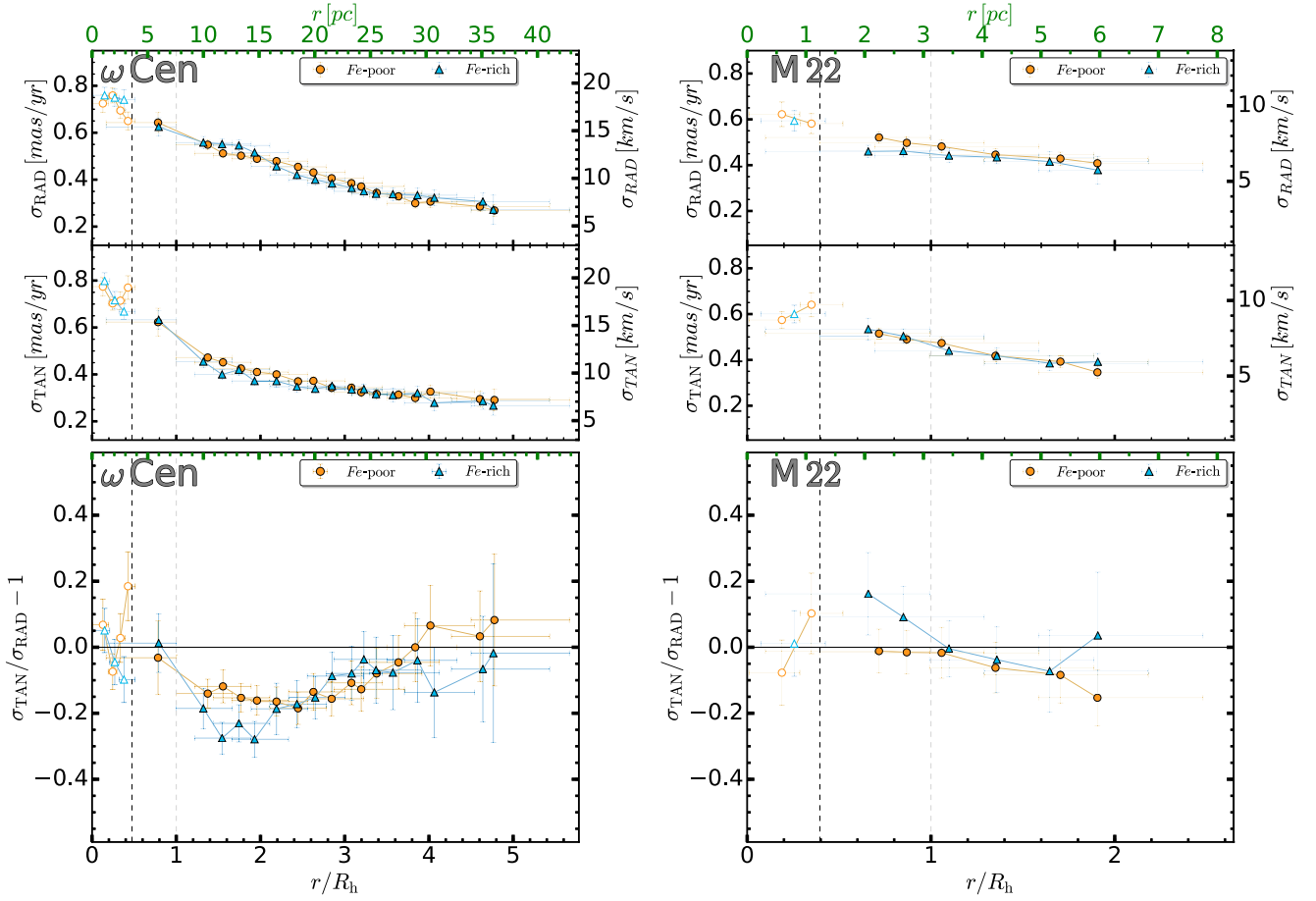
Figure 8. Velocity dispersion profiles for ω Centauri (top left) and M22 (top right). Empty markers are HST results, and filled markers correspond to Gaia DR2 proper motions. The bottom panels show the corresponding anisotropy radial profiles. The horizontal lines plotted in the bottom panels correspond to isotropic stellar systems. Orange circles and cyan triangles represent Fe-poor and Fe-rich stars, respectively. The black and gray vertical dashed lines highlight the core radii and the half-light radii of each cluster from Baumgardt & Hilker (2018). The radial quantity is normalized over the half-light radius.

Table 4
Third and Fourth Columns Indicate the Probability (p-value) that the Two Populations Come from the Same Parent Distribution, According to the A-D Test

Cluster		$\Delta\mu_{RAD}$ (A-D)	$\Delta\mu_{TAN}$ (A-D)	$\Delta\mu_{RAD}$ P	$\Delta\mu_{TAN}$ (P)	$\Delta\sigma_{RAD}$ (P)	$\Delta\sigma_{TAN}$ (P)	$\Delta\beta$ (P)
ω Centauri	Fe-poor−Fe-rich	0.100	0.110	$0.690_{0.999}^{0.230}$	$0.750_{0.989}^{0.660}$	$0.230_{0.026}^{0.026}$	$0.449_{0.012}^{0.012}$	$0.600_{0.030}^{0.030}$
	N-poor−N-rich	0.120	0.090	$0.619_{0.945}^{0.172}$	$0.866_{0.977}^{0.583}$	$0.412_{0.011}^{0.011}$	$0.151_{0.007}^{0.007}$	$0.555_{0.065}^{0.065}$
Fe-poor	N-poor−N-rich	0.180	0.130	$0.600_{0.970}^{0.186}$	$0.745_{0.980}^{0.237}$	$0.478_{0.957}^{0.004}$	$0.132_{0.909}^{0.021}$	$0.638_{0.916}^{0.040}$
Fe-rich	N-poor−N-rich	0.160	0.060	$0.378_{0.970}^{0.003}$	$0.186_{0.825}^{0.000}$	$0.400_{0.959}^{0.005}$	$0.280_{0.874}^{0.012}$	$0.514_{0.998}^{0.043}$
	N-poor−pop-a	0.023	0.020	$0.600_{0.884}^{0.416}$	$0.144_{0.809}^{0.066}$	$0.295_{0.447}^{0.216}$	$0.428_{0.385}^{0.026}$	$0.682_{0.976}^{0.346}$
	N-rich−pop-a	0.014	0.040	$0.650_{0.802}^{0.472}$	$0.201_{0.472}^{0.064}$	$0.850_{0.959}^{0.778}$	$0.446_{0.697}^{0.290}$	$0.388_{0.680}^{0.058}$
M22	Fe-poor−Fe-rich	0.201	0.015	$0.810_{0.988}^{0.587}$	$0.749_{0.976}^{0.509}$	$0.312_{0.644}^{0.009}$	$0.501_{0.997}^{0.104}$	$0.609_{0.920}^{0.231}$
	N-poor−N-rich	0.250	0.026	$0.772_{0.953}^{0.387}$	$0.709_{0.896}^{0.536}$	$0.460_{0.963}^{0.059}$	$0.504_{0.863}^{0.240}$	$0.587_{0.999}^{0.177}$

Note. We considered the radial distributions of the quantities listed in the first line: $\Delta\mu_{RAD}$, $\Delta\mu_{TAN}$, $\Delta\sigma_{RAD}$, $\Delta\sigma_{TAN}$, and $\Delta\beta$. The test has been carried out independently in the radial and tangential component. The remaining columns list the probability, P, that the velocity distributions come from the same parent distribution ($P = 1$) or not ($P = 0$), determined as described in Section 4.2.1. We provide the average value of P and the minimum and maximum p-values.

N-poor stars. Results on ω Centauri are illustrated in Figure 9 and 10.

The upper panels of Figure 9 compare the density contours of the overall N-poor and N-rich samples. Clearly, N-rich stars, which have average ellipticity, $e \sim 0.13$, exhibit more elliptical distributions than N-poor stars ($e \sim 0.05$).

The ellipticity difference between the spatial distributions of N-rich and N-poor stars is larger when we limit the analysis to the Fe-poor stars, as shown in the middle panels of Figure 9. Specifically, N-rich Fe-poor stars exhibit more flattened distributions (ellipticity $e \sim 0.20$) than N-poor Fe-poor stars, which have $e \sim 0.05$.
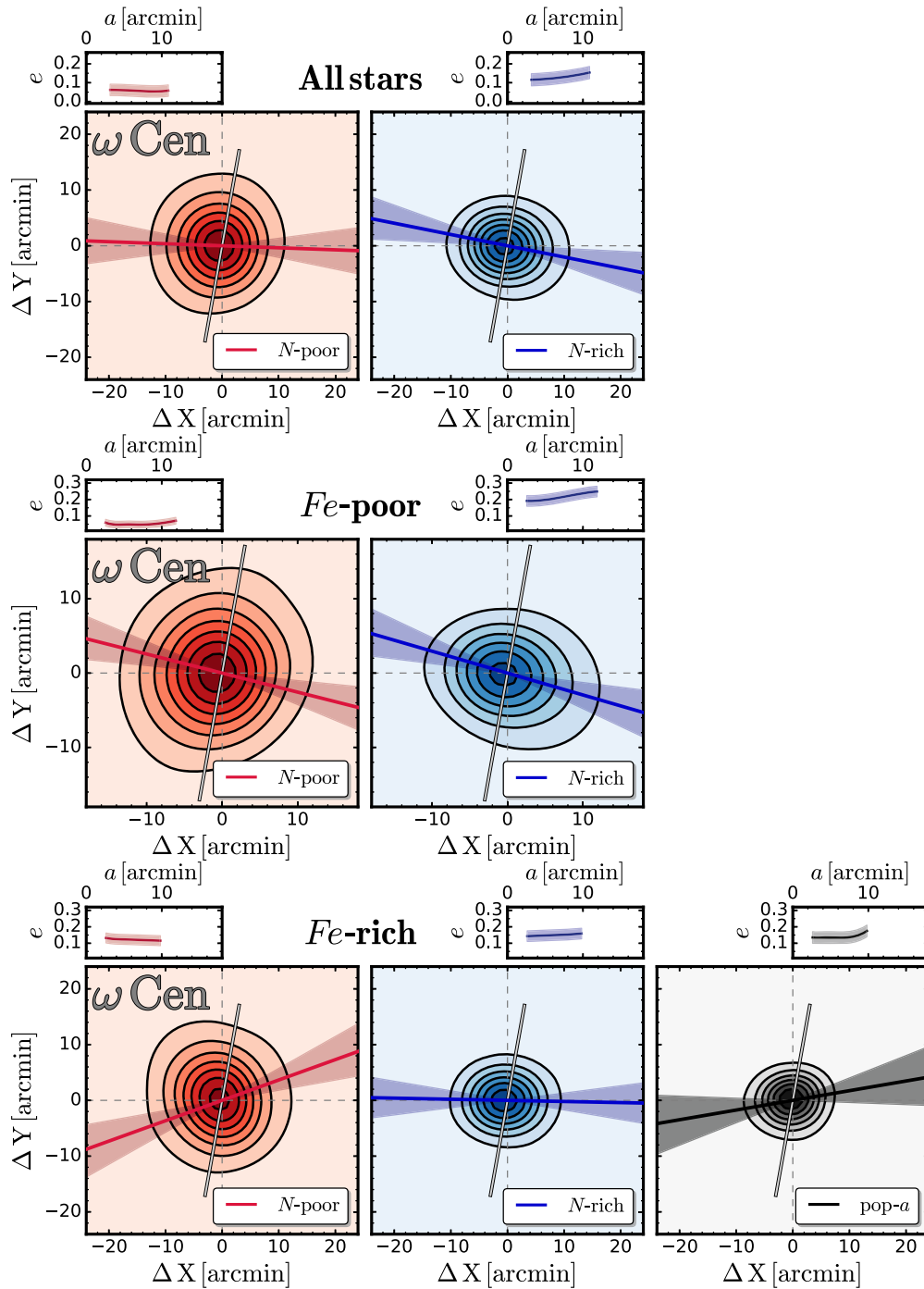
Figure 9. Density maps of stellar populations of ω Centauri with different nitrogen abundances and of population-a stars. The top and center rows refer to Fe-poor and Fe-rich stars, respectively, while the bottom panels show the spatial distribution of the entire sample of N-poor and N-rich stars. The ellipticities of the isodensity contours are plotted as a function of the semimajor axis.

Qualitatively, the spatial distributions of the Fe-rich subpopulations with different nitrogen abundances follow a similar behavior as their Fe-poor counterparts, although the ellipticity differences of the various subpopulations are less pronounced. Indeed, as shown in the lower panels of Figure 9, N-rich Fe-rich stars have an average ellipticity of $e \sim 0.15$, which is slightly higher than that of N-poor Fe-rich stars ($e \sim 0.12$). The ellipticity difference is significant at the $\sim 2.1\sigma$ level. On the other hand, population-a stars have, on average, $e \sim 0.13$, and the small ellipticity difference with N-rich Fe-rich and N-poor Fe-rich is not statistically significant.

Overall, Figure 9 reveals that the median semimajor axes of the best-fit ellipses of all populations are consistent with each other within one sigma and are almost perpendicular to the global rotation axis determined in Sollima et al. (2019).

For completeness, we plot the ellipticity of the various subpopulations as a function of the major axis of the best-fit ellipse, a, in the bottom panels of Figure 10. The upper panels show the absolute value of the ellipticity differences $|\Delta e|$ between the populations quoted in the figures against a. The color scale is indicative of the statistical significance of the
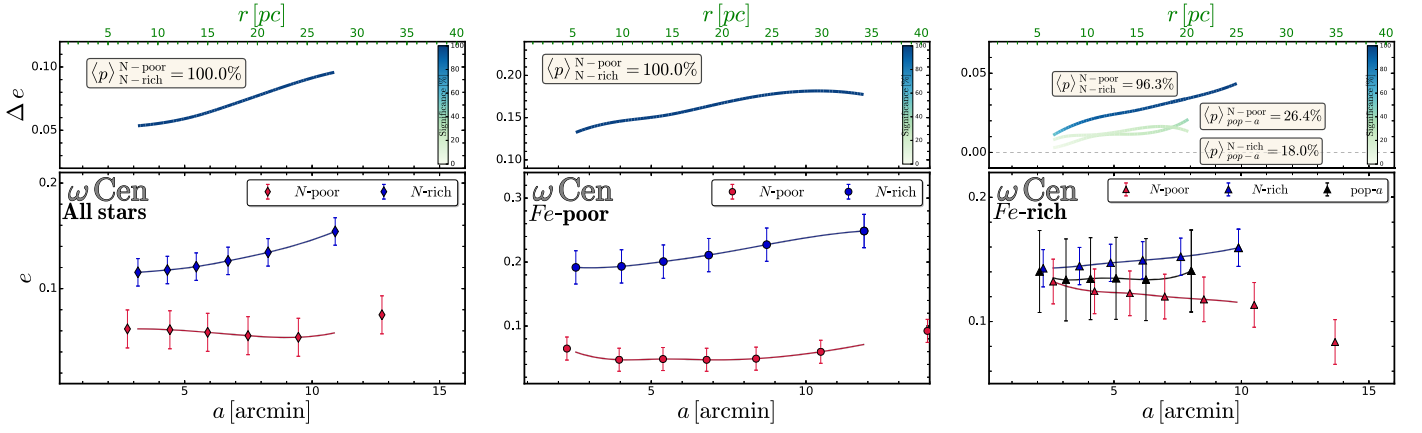
Figure 10. Lower panels: ellipticity of N-rich and N-poor stellar populations as a function of the major semiaxis of the best-fit ellipses, a for in the entire sample of analyzed ω Centauri stars (left), among Fe-poor stars (middle) and Fe-rich stars (right). The latter panel also includes population-a stars. Upper panels: absolute values of ellipticity differences inferred from the populations quoted in each panel against a. The color levels indicate the statistical significance of the difference as indicated by the color bar.
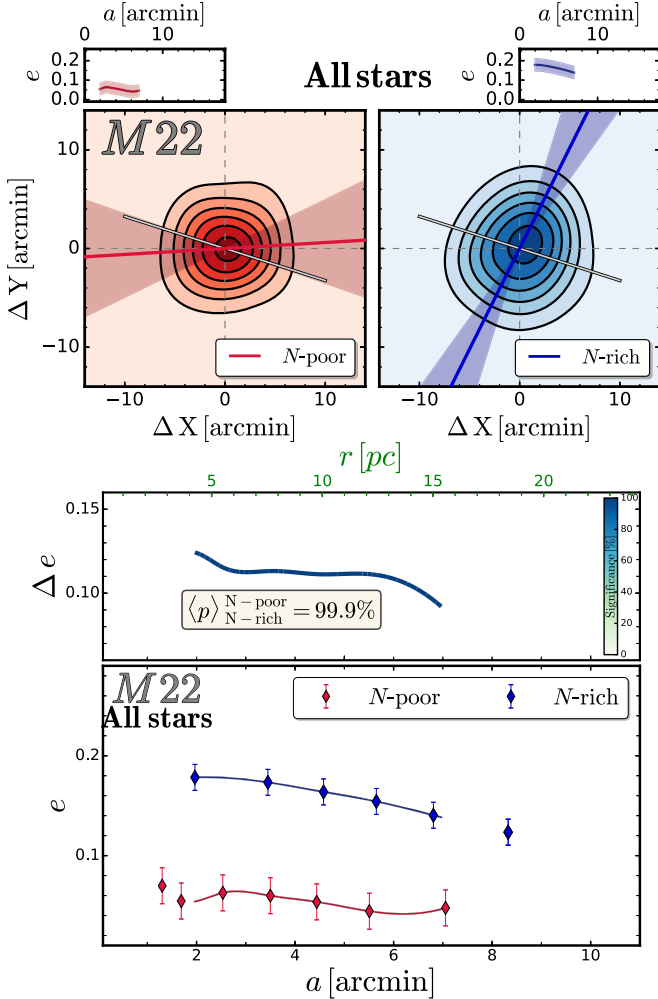
Figure 11. Top panels: same as Figures 3 and 9 for the N-poor (red, left panel) and N-rich (blue, right panel) populations in M22. Bottom panel: ellipticity profile as in Figures 4 and 10.

difference. All populations are consistent with having constant ellipticity in the analyzed interval of a.

Results on the spatial distributions of the N-poor and N-rich stellar populations of M22 are illustrated in Figure 11. N-rich stars have an average ellipticity $e \sim 0.15$ and clearly exhibit a flatter distribution than N-poor stars, which have $e \sim 0.05$.

5.2. Internal Kinematics

The internal kinematics of the stellar populations with different nitrogen abundances and of population-a stars are derived using the methods described in Section 4.3.

The velocity profiles of the entire sample of N-rich and N-poor stars are plotted in the left panels of Figure 12 and the corresponding results on the subpopulations of N-poor and N-rich populations among Fe-poor and Fe-rich stars are illustrated in the middle and right panels of Figure 12, respectively. The right panels also include the velocity profiles of population-a stars.

A visual inspection of the top left panels of Figure 12 reveals that both N-rich and N-poor stars exhibit significant rotation in the plane of the sky, with $\Delta\mu_{TAN}$ ranging from $\sim 6\,\mathrm{km\,s^{-1}}$ toward the cluster core to $\sim 2\,\mathrm{km\,s^{-1}}$ in the most distant regions.

Stellar populations with different nitrogen abundances exhibit radial anisotropic motions between ~ 1 and 3 half-light radii. Differences in the radial profile of β are present in the region with $r/R_{\mathrm{h}} \sim 1.5$–2.5, where the anisotropic motions of N-rich stars have more strongly radial and lie between ~ 3 and 4.5 half-light radii, where N-poor stars are consistent with having isotropic motions, while N-rich stars have $\beta \sim -0.2$.

When we consider the sample of Fe-poor stars alone, we find that N-poor and N-rich stars have similar rotation patterns. In contrast, stellar populations with different nitrogen abundances seem to exhibit different tangential velocity profiles in the radial annulus between ~ 0.8 and ~ 2.3 half-light radii.

The average values of $\Delta\mu_{TAN}$ for N-poor and N-rich stars, estimated as in Vasiliev (2019), are 0.27 ± 0.06 and 0.18 ± 0.06, respectively. However, these uncertainties, which account for systematic errors that affect Gaia DR2 proper motions, are upper limits to the true errors on the relative proper motions. Indeed, Gaia DR2 systematic errors depend on stellar colors and positions. Hence, they mostly cancel out when we consider the relative motions of N-rich and N-poor stars that have similar colors and spatial distributions. The average $\Delta\mu_{TAN}$ difference between N-poor and N-rich stars is 0.09 ± 0.03 when we do not consider the contribution of Gaia
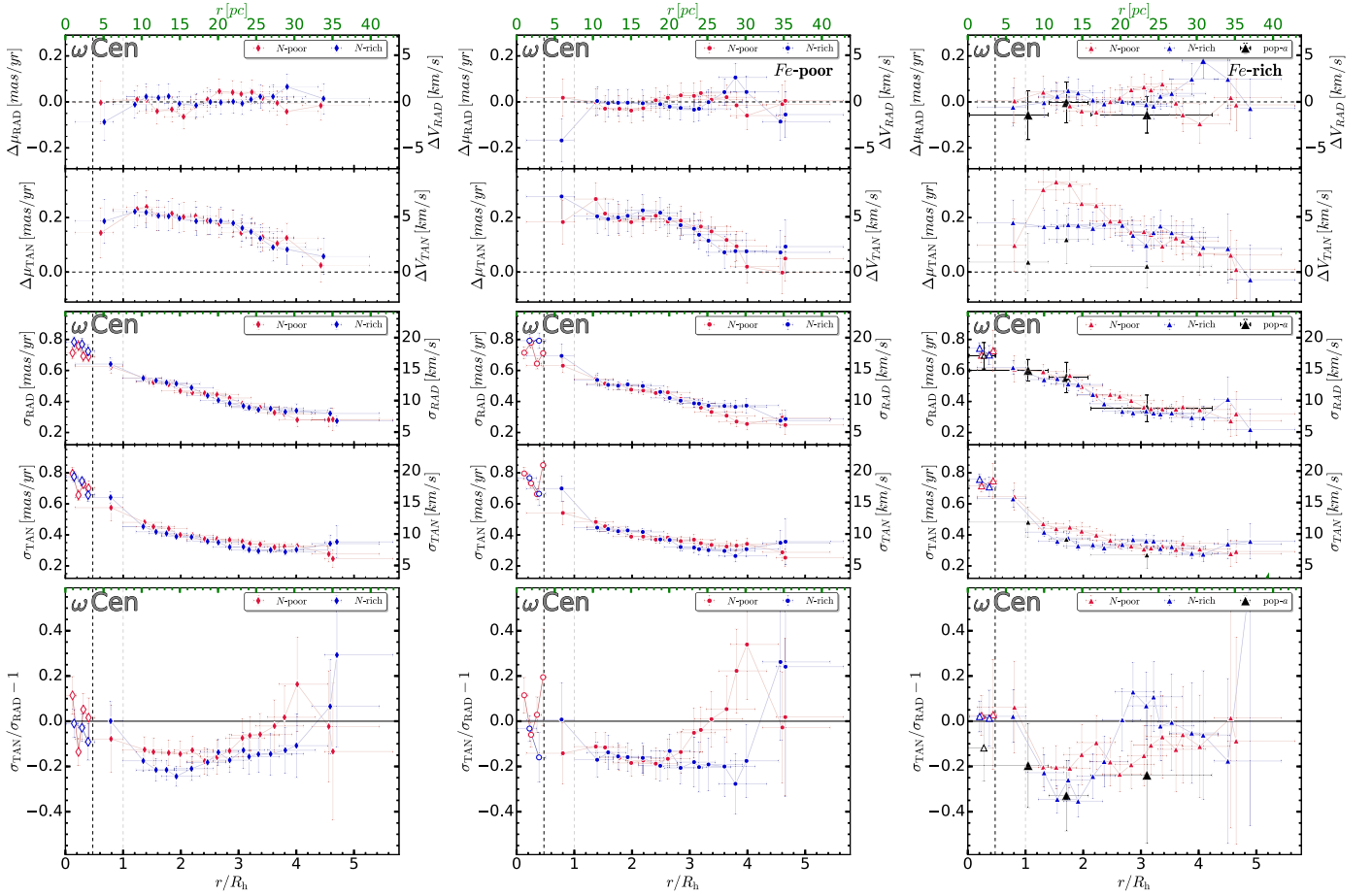
Figure 12. From top to bottom: average velocity, velocity dispersion, and anisotropy profiles as a function of the distance from the cluster center for N-poor (red dots) and N-rich (blue triangles) stars. the left panels refer to the entire sample of ω Centauri stars, and in the middle and right panels we considered the Fe-poor and Fe-rich populations, respectively. The velocity profiles of population-a stars are plotted with black triangles in the right panels. The black and gray vertical dashed lines highlight the core radius and the half-light radius from Baumgardt & Hilker (2018). The radial quantity is normalized over the half-light radius.

DR2 systematics. In this case, the difference would be significant at the 3σ level.

To further investigate the rotation of stellar populations with different nitrogen abundances in Fe-rich stars, we plot in Figure 13 $\Delta\mu_\alpha \cos\delta$ and $\Delta\mu_\delta$ as a function of θ for N-poor Fe-rich and N-rich Fe-rich stars in the two radial bins. We find that the rotation curves of N-poor stars within two half-light radii from the cluster center exhibit higher amplitudes than those of N-rich stars in the same radial bin. The amplitude differences derived from the $\Delta\mu_\alpha \cos\delta$ versus θ and $\Delta\mu_\delta$ versus θ planes are significant at 2.4σ and 2.1σ level, respectively. Hence, the probability that the amplitude differences that are observed in both components of proper motions are due to observational errors is lower than 0.2%. The rotation curves of the two populations are consistent with having the same amplitudes when we consider stars with $r > 2R_\mathrm{h}$.

6. Summary and Conclusions

We combined Gaia DR2 and HST proper motions with multiband photometry from HST and ground-based facilities to investigate the spatial distributions and the internal kinematics of multiple stellar populations in the Type II GCs M22 and ω Centauri over a wide field of view, from the cluster center up to ~2.5 and ~5.5 half-light radii, respectively.

We first identified stellar populations with different iron abundances along the RGB from differential-reddening corrected CMDs built with appropriate combinations of U, V, and I magnitudes (or m_{F336W}, m_{F606W}, m_{F814W} magnitudes, in the case of HST data). Then, we identified and analyzed stellar populations with different nitrogen content. The main results for stellar populations with different metallicities of M22 can be summarized as follows:

1. Fe-poor and Fe-rich stars exhibit the same average proper motions within 1σ. The same result is true for stellar populations with different nitrogen abundance.
2. Fe-poor and Fe-rich stars share similar spatial distributions with an average ellipticity, $e \sim 0.1$ (Figure 4).
3. Both populations exhibit significant rotation in the plane of the sky, and their rotation curves are characterized by similar phases and amplitudes ($A \sim 2.5\,\mathrm{km\,s^{-1}}$, Figure 6). The tangential velocity profiles of Fe-poor and Fe-rich stars are nearly flat in the analyzed radial interval, with an average $\Delta\mu_\mathrm{TAN} \sim 2.5\,\mathrm{km\,s^{-1}}$ (Figure 5).
4. Fe-poor and Fe-rich stars share similar velocity-dispersion profiles, with both the radial and tangential component ranging from ~9 to $\sim6\,\mathrm{km\,s^{-1}}$ when we move from the cluster center to a radius of ~2.5 half-light radii. Both populations exhibit isotropic motions (Figure 8).
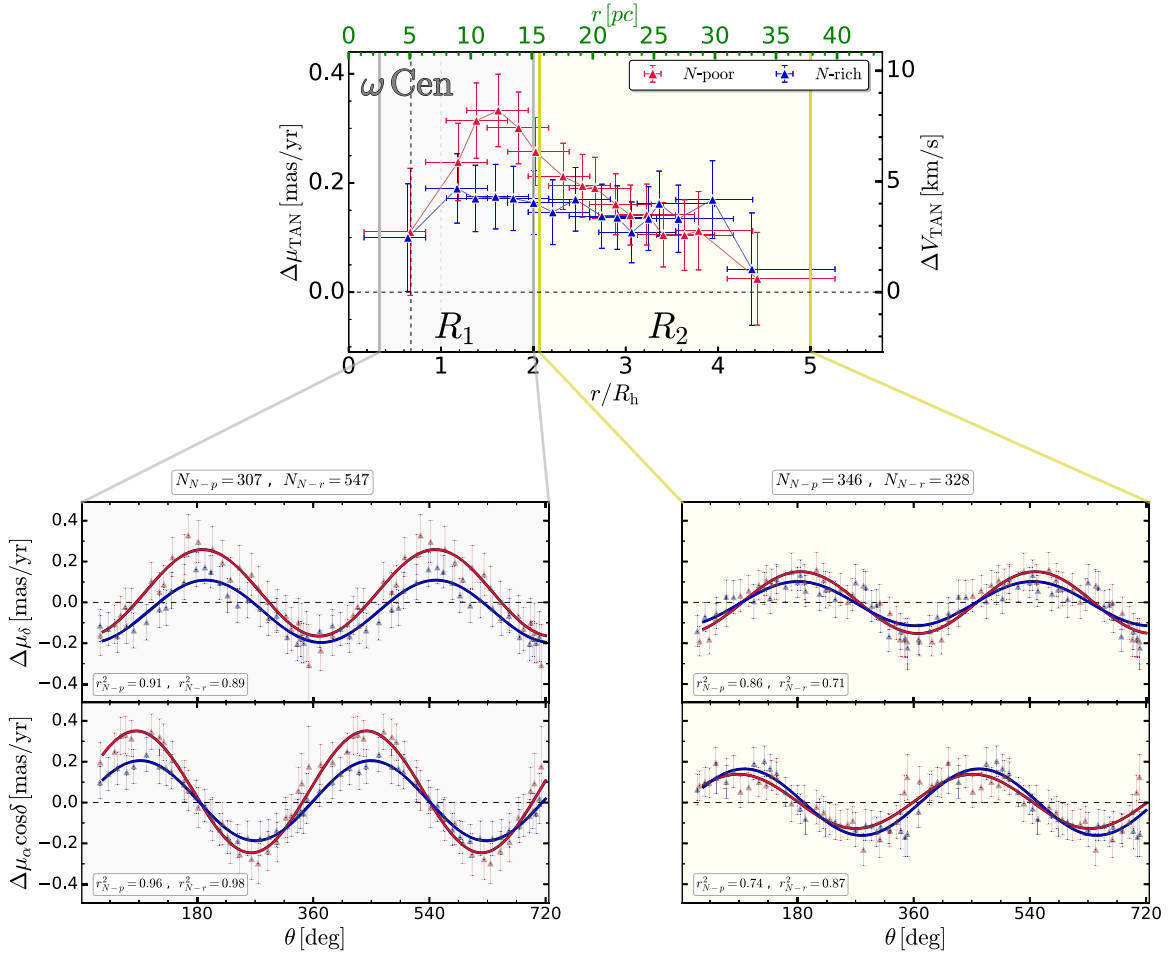
Figure 13. Reproduction of the radial profile of $\Delta\mu_{TAN}$ for the N-rich and N-poor groups of Fe-rich stars (top) in ωCen. In the bottom panels, $\Delta\mu_\alpha \cos\delta$ and $\Delta\mu_\delta$ are plotted as a function of the position angle θ for stars in regions R_1 and R_2 defined in the top panel. The sine functions that provide the best fit with the observations of N-poor and N-rich stars are represented with red and blue lines, respectively.

The main findings on the Fe-poor and Fe-rich stars of ω Centauri include the following aspects:

1. The stellar populations with different metallicities share the same motions, which confirms the conclusions by Anderson & van der Marel (2010) and Sanna et al. (2020). Similarly, stellar populations with different N have the same average proper motions.

2. The spatial distributions of both stellar populations have similar elliptical shapes with ellipticity, $e \sim 0.06$, and similar directions of the major axes (Figure 4).

3. The rotation pattern in the plane of the sky is similar for Fe-poor and Fe-rich stars. The tangential velocity component decreases from $\sim 6\,\mathrm{km\,s^{-1}}$ at a radial distance of about one half-light radius from the center to $\sim 2\,\mathrm{km\,s^{-1}}$ at $r/R_h \sim 5$ (Figure 5 and 6).

4. The rotation curves of both populations share similar amplitudes and phases. When we investigate regions with different radial distances from the cluster center, we find that the amplitude of the rotation decreases when we move away from the cluster center (Figure 7).

5. Both populations exhibit similar velocity-dispersion profiles in the plane of the sky, with the values of radial and tangential velocities ranging from $\sim 18\,\mathrm{km\,s^{-1}}$ in the

cluster center to $7\,\mathrm{km\,s^{-1}}$ at a distance of $\sim 5\,\mathrm{km\,s^{-1}}$ (Figure 8).

6. The motions of the stellar populations with different metallicities are isotropic within about one half-light radius from the cluster center and radially anisotropic from ~ 1 up to $\sim 4\,R_h$ (Figure 8). The motions become isotropic in the outermost regions.

In addition, we identified two main groups of N-poor and N-rich stars of both ω Centauri and M22 and studied their spatial distributions and internal kinematics. In the case of ω Centauri, we also investigated the population-a, which is composed of the most metal-rich stars of this cluster (e.g., Johnson & Pilachowski 2010; Marino et al. 2011).

The main results for stellar populations with different nitrogen in ω Centauri can be summarized as follows:

1. N-rich stars of ω Centauri exhibit a flatter spatial distribution than N-poor stars. The difference is more pronounced when we consider the sample of metal-poor stars alone, where the N-poor Fe-poor and N-rich Fe-poor subpopulations have average ellipticities of ~ 0.06 and ~ 0.22, respectively (Figure 10). Population-a stars exhibit higher ellipticity ($e \sim 0.13$) than the bulk of ω Centauri stars, which have $e \sim 0.07$.

2. N-poor and N-rich stars of ω Centauri exhibit similar rotation patterns. However, when we consider the Fe-rich population alone, we find that N-rich Fe-rich stars have lower tangential velocities than N-poor Fe-poor stars in the radial interval between about one and about three half-light radii (Figure 12). In this region, the amplitude of the rotation curve of N-rich Fe-rich stars of ω Centauri seems smaller than that of N-poor Fe-rich stars, but the amplitude difference is only significant at the $\sim 2.4\sigma$ and 2.1 level when we consider the motions $\Delta\mu_\alpha \cos\delta$ versus θ and $\Delta\mu_\delta$ versus θ planes, respectively. Therefore, the probability that the amplitude differences are due to observational uncertainties in both components at the same time is smaller than 0.002. Similarly to the group of N-rich Fe-rich stars, population-a seems to exhibit low values of $\Delta\mu_{\rm TAN}$ relative to the N-poor Fe-poor stars.[7]

3. Both N-rich and N-poor stars of ω Centauri exhibit radially anisotropic motions with some indications for differences between the level of anisotropy of the two populations in the radial interval between 1.5 and 2.5 half-light radii. Between ~ 3 and 4.5 half-light radii, N-poor stars are consistent with isotropic motions, while N-rich stars have $\beta \sim -0.2$ (Figure 12).

Numerical studies show that tidally filled stellar systems exhibit isotropic motions in their central regions as a consequence of the shorter relaxation time and the high stellar encounter rate. When it moves toward the middle regions, the system starts to expand due to the relaxation process. Therefore, stars in these regions would exhibit a moderate radially anisotropic motion. Finally, because stars with radial orbits preferentially escape from the system (e.g., Takahashi et al. 1997), the outermost regions are characterized by isotropic motions. On the other hand, tidally underfilling systems do not show an isotropic pattern in the outer regions (Vesperini et al. 2014; Tiongco et al. 2016).

Based on N-body simulations of multiple populations in GCs, Tiongco et al. (2019) show that the anisotropy profile of 1G[8] stars evolves as a tidally filling stellar system, whereas 2G stars behave like a tidally underfilling system (see also Tiongco et al. 2016). Hence, their 1G and 2G stars share similar anisotropy profiles in the inner and middle regions of the clusters, but exhibit different trends in the outer regions. The anisotropy profiles of N-poor Fe-poor and N-rich Fe-poor stars (bottom middle panel of Figure 12) are qualitatively consistent with the findings by Tiongco and collaborators. Similar conclusions are drawn by Bellini et al. (2015) in their investigation of the internal kinematics of stellar populations in the GC NGC 2808.

We find that the ellipses that reproduce the distribution of N-rich stars of M22 have higher ellipticities than those of N-poor stars, in close analogy with what is observed in ω Centauri. This result is qualitatively consistent with the conclusion by Lee (2015), who find that Ca-rich stars of M22 are more elongated than Ca-poor stars under the hypothesis that Ca-rich stars are on average nitrogen enhanced with respect to the Ca-poor population. N-poor and N-rich stars of M22 exhibit similar rotation patterns and radially isotropic proper motions. The fact that M22 has significantly shorter relaxation times than ω Centauri (e.g., Baumgardt & Hilker 2018) could indicate that M22 stars are partially mixed and have erased most of the initial dynamical differences between the distinct stellar populations. This possibility could explain why the stellar populations of M22 share the similar kinematics. However, it is worth noting that our results do not confirm the conclusion by Lee (2015, 2020), who find metal-rich stars of M22 rotate faster than metal-poor stars both in the plane of the sky and along the line of sight.

The results ore based on the selection of Fe-rich and Fe-poor stars derived from the procedure I of Section 3. We repeated the analysis by using the sample of Fe-rich and Fe-poor stars of ω Centauri selected by using procedures II and III of Section 3 and confirm all the conclusions of the paper. We conclude that the results are not affected by the criteria we adopted to separate stars with different metallicities.

The findings of this paper, together with results from the literature, provide constraints on the formation and evolution of multiple populations in Type II GCs. Indeed, the present-day dynamics of stellar populations in clusters where the stars are not fully mixed provides information on the initial conditions of stellar populations in GCs.

In this context, we emphasize that the rotation of stellar populations with different metallicities has previously been studied based on radial velocities of RGB stars. In their spectroscopic study of ~ 400 stars in ω Centauri, Norris et al. (1997) did not find significant rotation along the line of sight in the most metal-rich stars in their sample (corresponding to $\sim 20\%$ of the studied stars). In contrast, the metal-poor component clearly exhibits systemic rotation. This result has been challenged by Pancino et al. (2007), who concluded that the metal-poor, metal-intermediate, and metal-rich stars are consistent with having the same rotation patterns based on radial velocities.

Our results on the rotation in the groups of Fe-poor and Fe-rich stars corroborate the evidence that the two main sample of stars with different metallicities share similar rotation patterns both along the line of sight and in the plane of the sky. However, the fact that the sample of population-a stars studied in this paper exhibit lower tangential velocities than the bulk of ω Centauri stars suggests that the stars of this extreme population, similarly to the other Fe-rich and N-rich stars of ω Centauri, exhibit less pronounced rotation in the plane of the sky than the remaining cluster members, similarly to what has been suggested by Norris et al. (1997) based on stellar radial velocities.

The motions on the plane of the sky of ω Centauri stars have recently been studied by using HST relative proper motions of stars in a field located $\sim 17'$ southwest of the cluster center (Bellini et al. 2018). The two groups of MS-I and MS-II stars studied by Bellini et al. (2018) can be tentatively associated

---

[7] The origin of population-a stars, which exhibit a metallicity that is different than that of the bulk of ω Centauri stars, is still widely debated. Work based on chemical evolution models suggests that it is an extreme case of chemical enrichment (e.g., D'Antona et al. 2011, and references therein). As an alternative, recent work suggests that it could be the product of a merger (Calamida et al. 2020). Specifically, the latter hypothesis would be supported by a strong radial anisotropy of population-a stars, which is a signature of a minor-merger remnant (Hong et al. 2017). Nevertheless, the fact that population-a stars are more centrally concentrated than metal-poor stars (e.g., Bellini et al. 2009) would be a challange for the merging scenario (Gavagnin et al. 2016).

[8] We adopt here the same naming convention as was used in Tiongco et al. (2019), i.e., 1G and 2G in place of 1P and 2P.

with the populations of N-poor and N-rich stars analyzed in our paper.[9] Bellini et al. (2018) showed that MS-II stars are significantly more radially anisotropic than MS-I stars, which are consistent with an isotropic velocity distribution. This result is consistent with our finding that at $r/R_{\rm h} \sim 3.5$ the N-rich stars have $\beta \sim -0.2$, while N-poor stars exhibit nearly isotropic motions. Moreover, MS-I stars exhibit excess systemic rotation in the plane of the sky with respect to MS-II stars (Bellini et al. 2018). In this paper, we find that among Fe-rich stars, the rotation curves of the N-poor population exhibit larger amplitudes than those of N-rich stars. Hence, both results from this paper and from Bellini and collaborators corroborate the conclusion that stellar populations with different nitrogen abundances exhibit distinct rotation patterns.

A variety of scenarios predict that GCs have experienced a complex formation history and that the multiple stellar populations are a consequence of different star formation episodes (Renzini et al. 2015, and references therein). According to some of these scenarios, GCs host second stellar generations that formed in high-density subsystems embedded in a more extended first generation (e.g., Ventura et al. 2001; D'Ercole et al. 2008; D'Antona et al. 2016; Calura et al. 2019). These scenarios are supported by the evidence that metal-rich and helium-rich stars of ω Centauri, whose half-light relaxation time exceeds the Hubble time, are more centrally concentrated than the bulk of cluster stars (e.g., Norris et al. 1996; Sollima et al. 2007; Bellini et al. 2009).
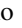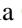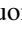
Mastrobuono-Battisti & Perets (2013, 2016) investigated the possibility that the formation of second-generation stars in GCs may occur in flattened and centrally concentrated disk-like structures. They used N-body simulations to explore the evolution of such stellar disks embedded in first-generation stars and concluded that the signature of the initial configuration can still be observable in the present-day clusters if the relaxation time is long enough. The finding that N-rich stars exhibit elliptical spatial distributions with higher eccentricity than that of N-poor stars is qualitatively consistent with the possibility that N-rich stars are the second generation of ω Centauri and formed a disk-like structure.

Based on the chemical composition of the stellar populations of ω Centauri, Marino et al. (2012) suggested that ω Centauri has first experienced the enrichment in iron and α elements (oxygen) from core-collapse supernovae. This process is followed by the formation of stellar populations from material ejected from more massive first-generation stars, possibly in the asymptotic giant branch phase, and processed by p-capture elements. The evidence that the groups of Fe-rich and Fe-poor stars of both ω Centauri and M22 have similar spatial distributions while N-rich stars are more flattened than N-poor stars is consistent with a scenario where distinct processes are responsible for the enrichment in iron and in p-capture elements, and where the formation of N-rich stellar populations is associated with the cooling flow of material in centrally concentrated disk-like structures.

ORCID iDs

G. Cordoni   https://orcid.org/0000-0002-7690-7683
A. P. Milone   https://orcid.org/0000-0001-7506-930X
A. F. Marino   https://orcid.org/0000-0002-1276-5487
G. S. Da Costa   https://orcid.org/0000-0001-7019-649X
H. Jerjen   https://orcid.org/0000-0003-4624-9592
E. P. Lagioia   https://orcid.org/0000-0003-1713-0082
A. Mastrobuono-Battisti   https://orcid.org/0000-0002-2386-9142
J. E. Norris   https://orcid.org/0000-0002-7900-5554
D. Yong   https://orcid.org/0000-0002-6502-1406

References

Anderson, J., Sarajedini, A., Bedin, L. R., et al. 2008, AJ, 135, 2055
Anderson, J., & van der Marel, R. P. 2010, ApJ, 710, 1032
Baumgardt, H., & Hilker, M. 2018, MNRAS, 478, 1520
Bekki, K., & Freeman, K. C. 2003, MNRAS, 346, L11
Bellazzini, M., Ibata, R. A., Chapman, S. C., et al. 2008, AJ, 136, 1147
Bellini, A., Anderson, J., Bedin, L. R., et al. 2011, PASP, 123, 622
Bellini, A., & Bedin, L. R. 2009, PASP, 121, 1419
Bellini, A., Libralato, M., Bedin, L. R., et al. 2018, ApJ, 853, 86
Bellini, A., Piotto, G., Bedin, L. R., et al. 2009, A&A, 493, 959
Bellini, A., Vesperini, E., Piotto, G., et al. 2015, ApJL, 810, L13
Bianchini, P., Ibata, R., & Famaey, B. 2019, ApJL, 887, L12
Bianchini, P., van der Marel, R. P., del Pino, A., et al. 2018, MNRAS, 481, 2125
Calamida, A., Zocchi, A., Bono, G., et al. 2020, ApJ, 891, 167
Calura, F., D'Ercole, A., Vesperini, E., et al. 2019, MNRAS, 489, 3269
Carretta, E., Bragaglia, A., Gratton, R. G., et al. 2009, A&A, 505, 117
Cordoni, G., Milone, A. P., Marino, A. F., et al. 2018, ApJ, 869, 139
Cordoni, G., Milone, A. P., Mastrobuono-Battisti, A., et al. 2020, ApJ, 889, 18
Da Costa, G. S., Held, E. V., Saviane, I., & Gullieuszik, M. 2009, ApJ, 705, 1481
Da Costa, G. S., & Marino, A. F. 2011, PASA, 28, 28
D'Antona, F., D'Ercole, A., Marino, A. F., et al. 2011, ApJ, 736, 7
D'Antona, F., Vesperini, E., D'Ercole, A., et al. 2016, MNRAS, 458, 2122
D'Ercole, A., Vesperini, E., D'Antona, F., et al. 2008, MNRAS, 391, 825
Gaia Collaboration, Brown, A. G. A., Vallenari, A., et al. 2018, A&A, 616, A1
Gavagnin, E., Mapelli, M., & Lake, G. 2016, MNRAS, 461, 1276
Halır, R., & Flusser, J. 1998, in Proc. 6th Int. Conf. in Central Europe on Computer Graphics and Visualization, 125, http://citeseerx.ist.psu.edu/viewdoc/download?doi=10.1.1.1.7559&rep=rep1&type=pdf
Harris, W. E. 1996, AJ, 112, 1487
Hénault-Brunet, V., Gieles, M., Agertz, O., & Read, J. I. 2015, MNRAS, 450, 1164

---

[9] MS-I and MS-II stars have been identified by Milone et al. (2017) throughout the entire MS, from the turnoff toward the hydrogen-burning limit, using optical and near-infrared HST photometry. MS-I stars are consistent with having average [Fe/H]~ -1.7 and primordial helium content, whereas MS-II stars are, on average, more metal rich ([Fe/H]~ -1.4) and have a high helium abundance ($Y \sim 0.37$–0.40). Both MSs host stellar subpopulations with different metallicities and light-element abundances, with MS-II stars having lower oxygen and higher nitrogen content than MS-I stars. Due to the complexity of ω Centauri, it is not possible to connect the stellar populations analyzed in this paper along the RGB with those identified by Milone et al. (2017) along the MS. Nevertheless, based on the metallicities and the content of helium and nitrogen, we can associate the bulk of MS-I stars with the N-poor population of this paper, whereas the majority of MS-II stars are the RGB counterparts of the N-rich population.

Cordoni et al.

Hong, J., de Grijs, R., Askar, A., et al. 2017, MNRAS, 472, 67
Johnson, C. I., & Pilachowski, C. A. 2010, ApJ, 772, 1373
Johnson, C. I., Rich, R. M., Pilachowski, C. A., et al. 2015, AJ, 150, 63
Landolt, A. U. 1992, AJ, 104, 340
Lee, J.-W. 2015, ApJS, 219, 7
Lee, J.-W. 2020, ApJL, 880, L6
Lee, Y. W., Joo, J. M., Sohn, Y. J., et al. 1999, Natur, 402, 55
Lindegren, L., Hernández, J., Bombrun, A., et al. 2018, A&A, 616, A2
Mackey, A. D., Da Costa, G. S., Ferguson, A. M. N., & Yong, D. 2013, ApJ, 762, 65
Marino, A. F., Milone, A. P., Karakas, A. I., et al. 2015, MNRAS, 450, 815
Marino, A. F., Milone, A. P., Piotto, G., et al. 2009, A&A, 505, 1099
Marino, A. F., Milone, A. P., Piotto, G., et al. 2012, ApJ, 746, 14
Marino, A. F., Milone, A. P., Renzini, A., et al. 2019, MNRAS, 487, 3815
Marino, A. F., Milone, A. P., Yong, D., et al. 2014, MNRAS, 442, 3044
Marino, A. F., Piotto, G., Gratton, R., et al. 2010, in IAU Symp. 268, Light Elements in the Universe, ed. C. Charbonnel et al. (Cambridge: Cambridge Univ. Press), 183
Marino, A. F., Sneden, C., Kraft, R. P., et al. 2011, A&A, 532, A8
Mastrobuono-Battisti, A., & Perets, H. B. 2013, ApJ, 779, 85
Mastrobuono-Battisti, A., & Perets, H. B. 2016, ApJ, 823, 61
Milone, A. P., Bedin, L. R., Piotto, G., et al. 2008, ApJ, 673, 241
Milone, A. P., Marino, A. F., Da Costa, G. S., et al. 2020, MNRAS, 491, 515
Milone, A. P., Marino, A. F., Mastrobuono-Battisti, A., & Lagioia, E. P. 2018, MNRAS, 479, 5005
Milone, A. P., Marino, A. F., Piotto, G., et al. 2015, ApJ, 808, 51
Milone, A. P., Piotto, G., Bedin, L. R., et al. 2012, A&A, 540, A16
Milone, A. P., Piotto, G., Renzini, A., et al. 2017, MNRAS, 464, 3636
Monelli, M., Milone, A. P., Stetson, P. B., et al. 2013, MNRAS, 431, 2126
Norris, J. E., Freeman, K. C., Mayor, M., et al. 1997, ApJL, 487, L187
Norris, J. E., Freeman, K. C., & Mighell, K. J. 1996, ApJ, 462, 241
Pancino, E., Ferraro, F. R., Bellazzini, M., et al. 2000, ApJL, 533, L83
Pancino, E., Galfo, A., Ferraro, F. R., et al. 2007, ApJL, 661, L155
Piotto, G., Milone, A. P., Anderson, J., et al. 2012, ApJ, 760, 39
Renzini, A., D'Antona, F., Cassisi, S., et al. 2015, MNRAS, 454, 4197
Sabbi, E., Lennon, D. J., Anderson, J., et al. 2016, ApJS, 222, 11
Sanna, N., Pancino, E., Zocchi, A., et al. 2020, A&A, 637, A46
Silverman, B. W. 1986, Monographs on Statistics and Applied Probability (London: Chapman and Hall)
Sollima, A., Baumgardt, H., & Hilker, M. 2019, MNRAS, 485, 1460
Sollima, A., Ferraro, F. R., Bellazzini, M., et al. 2007, ApJ, 654, 915
Stetson, P. B. 2005, PASP, 117, 563
Stetson, P. B., Pancino, E., Zocchi, A., et al. 2019, MNRAS, 485, 3042
Takahashi, K., Lee, H., & Inagaki, S. 1997, MNRAS, 292, 331
Tiongco, M. A., Vesperini, E., & Varri, A. L. 2016, MNRAS, 455, 3693
Tiongco, M. A., Vesperini, E., & Varri, A. L. 2019, MNRAS, 487, 5535
van de Ven, G., van den Bosch, R. C. E., Verolme, E. K., & de Zeeuw, P. T. 2006, A&A, 445, 513
Vasiliev, E. 2019, MNRAS, 484, 2832
Ventura, P., D'Antona, F., Mazzitelli, I., & Gratton, R. 2001, ApJL, 550, L65
Vesperini, E., McMillan, S. L. W., D'Antona, F., & D'Ercole, A. 2013, MNRAS, 429, 1913
Vesperini, E., Varri, A. L., McMillan, S. L. W., & Zepf, S. E. 2014, MNRAS, 443, 79
Wand, M. 2015, KernSmooth: Functions for Kernel Smoothing Supporting Wand & Jones (1995), R package v2.23-16, https://CRAN.R-project.org/package=KernSmooth
Yong, D., & Grundahl, F. 2008, ApJ, 672, 29
Yong, D., Roederer, I. U., Grundahl, F., et al. 2014, MNRAS, 441, 3396